GLOBAL BIOGEOCHEMICAL CYCLES, VOL. 15, NO. 4, PAGES 891–907, DECEMBER 2001

Global warming feedbacks on terrestrial carbon uptake under the Intergovernmental Panel on Climate Change (IPCC) emission scenarios

Fortunat Joos,[1] I. Colin Prentice,[2] Stephen Sitch,[3] Robert Meyer,[1] Georg Hooss,[4] Gian-Kasper Plattner,[1] Stefan Gerber,[1] and Klaus Hasselmann[4]

Abstract. A coupled physical-biogeochemical climate model that includes a dynamic global vegetation model and a representation of a coupled atmosphere-ocean general circulation model is driven by the nonintervention emission scenarios recently developed by the Intergovernmental Panel on Climate Change (IPCC). Atmospheric CO_2, carbon sinks, radiative forcing by greenhouse gases (GHGs) and aerosols, changes in the fields of surface-air temperature, precipitation, cloud cover, ocean thermal expansion, and vegetation structure are projected. Up to 2100, atmospheric CO_2 increases to 540 ppm for the lowest and to 960 ppm for the highest emission scenario analyzed. Sensitivity analyses suggest an uncertainty in these projections of −10 to +30% for a given emission scenario. Radiative forcing is estimated to increase between 3 and 8 W m^{-2} between now and 2100. Simulated warmer conditions in North America and Eurasia affect ecosystem structure: boreal trees expand poleward in high latitudes and are partly replaced by temperate trees and grasses at lower latitudes. The consequences for terrestrial carbon storage depend on the assumed sensitivity of climate to radiative forcing, the sensitivity of soil respiration to temperature, and the rate of increase in radiative forcing by both CO_2 and other GHGs. In the most extreme cases, the terrestrial biosphere becomes a source of carbon during the second half of the century. High GHG emissions and high contributions of non-CO_2 agents to radiative forcing favor a transient terrestrial carbon source by enhancing warming and the associated release of soil carbon.

1. Introduction

The urgency of climate policy actions depends on how future concentrations of greenhouse gases (GHGs) and global climate change are likely to evolve in the absence of GHG emission control and how global climate change may affect the world's ecosystems and the services they provide. Carbon dioxide (CO_2) is the most important anthropogenic greenhouse gas (GHG). Currently, only about half of the anthropogenic CO_2 emission stays airborne. The rest is taken up by the terrestrial biosphere and the ocean. Global climate change due to increased GHG concentrations has the potential to reduce these natural CO_2 sinks [e.g., *Cao and Woodward*, 1998; *Sarmiento and Le Quéré*, 1996; *Joos et al.*, 1999b; *Cramer et al*., 2000] and to affect ecosystem structure [*Smith and Shugart*, 1993] in ways that could enhance or reduce carbon uptake [*Cramer et al.*, 2001; *Smith and Shugart*, 1993; *Cox et al.*, 2000]. However, projections of future atmospheric CO_2 and climate are rendered uncertain by our understanding of how the mechanisms driving oceanic and terrestrial carbon sequestration are influenced by a changing environment.

We investigated possible feedbacks between global climate change and the terrestrial system and their impacts on projections of future changes in climate and ecosystem structure for the new emission scenarios developed by the writing team of the Intergovernmental Panel on Climate Change (IPCC) Special Report on Emission Scenarios (SRES) [*Nakićenović et al.*, 2000]. The feedbacks involve atmospheric CO_2, other radiative forcing agents, changes in surface temperature, the hydrological cycle, and the carbon cycle. Rising atmospheric concentrations of CO_2 and other GHGs lead to increased radiative forcing, higher surface-air temperatures, and changes in the hydrological cycle [*Houghton et al.*, 1996]. Such changes may cause increased respiration of the carbon stored in soil and litter owing to higher bacterial activities at higher temperatures [*Lloyd and Taylor*, 1994; *Rustad*, 2000; *Cox et al.*, 2000], reduced net primary production because of excessively high temperatures and/or reduced water availability [*Cramer et al.*, 2001], and dieback of extant forests in response to heat or drought stress [*Cramer et al.*, 2001; *Smith and Shugart*, 1993; *Cox et al.*, 2000], thereby offsetting the carbon uptake stimulated by the increase in atmospheric CO_2 [*Farquhar et al.*, 1980] and, in some regions, by climate change. Although there is still considerable uncertainty about the relative magnitudes of these processes, paleodata clearly indicate that terrestrial carbon storage has varied under different climatic regimes [e.g., *Crowley*, 1995] and that the terrestrial system can show a substantial response to climatic shifts within a few decades [e.g., *MacDonald et al.*, 1993; *Mayle and Cwyner*, 1995; *Birks and Ammann*, 2000].

Most modeling studies to date have only partly addressed the feedback loops described above by prescribing atmospheric CO_2 and climate in dynamic global vegetation models (DGVMs) [*Cramer et al.*, 2001] or in simpler terrestrial carbon models that prescribe the ecosystem distribution as constant in time [*Cao and Woodward*, 1998; *Meyer et al.*, 1999]. These studies show that the

[1]Climate and Environmental Physics, Bern, Switzerland.
[2]Max Planck Institute for Biogeochemistry, Jena, Germany.
[3]Potsdam Institute for Climate Impact Research, Potsdam, Germany.
[4]Max Planck Institute for Meteorology, Hamburg, Germany.

Paper number 2000GB001375.
0886-6236/01/2000GB001375$12.00

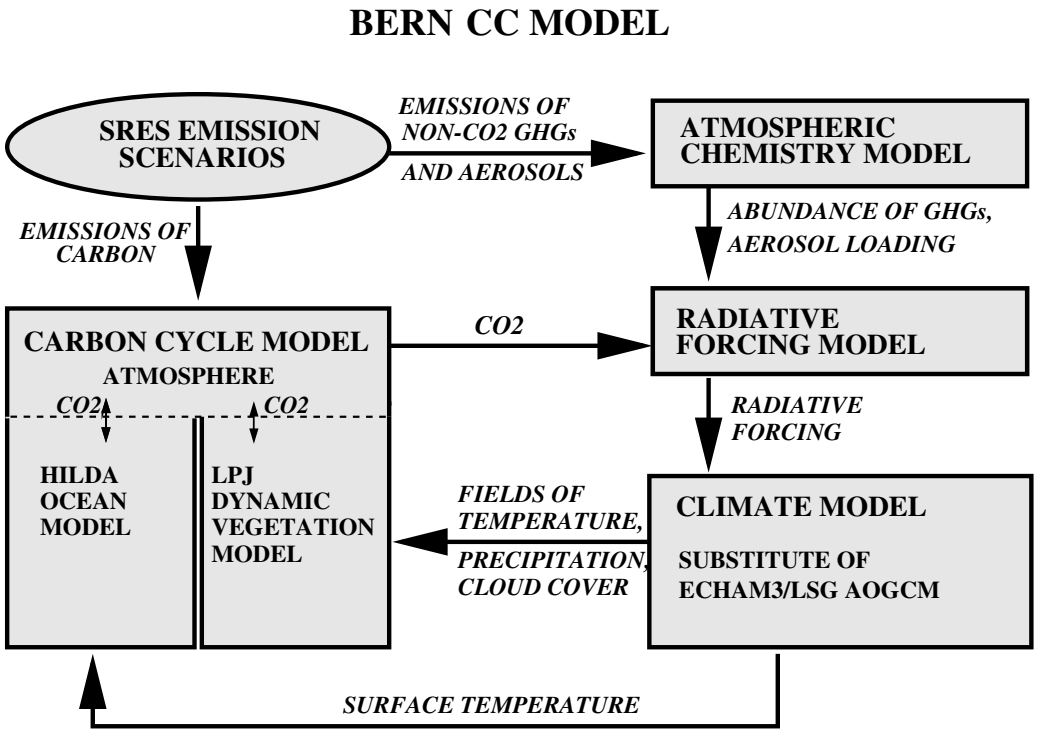

Figure 1. Simplified scheme of the Bern CC model. For scenario calculations, future abundances of greenhouse gases (GHGs) are projected from the emissions of CO_2 and non-CO_2 GHGs. Radiative forcing is calculated from the abundance of CO_2 and non-CO_2 GHGs and emissions of aerosol precursors. The IRF-EOF substitute of the ECHAM3/LSG AOGCM is driven by radiative forcing, and modeled surface fields of temperature, precipitation, and cloud cover are passed to the carbon cycle model. The carbon cycle model includes a well-mixed atmosphere, the HILDA ocean model, and the Lund-Potsdam-Jena (LPJ) Dynamic Global Vegetation Model. Atmospheric CO_2 is projected from carbon emissions by fossil fuel burning and land use changes and the carbon uptake (release) by the ocean and the land biosphere.

terrestrial sink is reduced in simulations considering climate change as compared to simulations without future climatic changes. Recently, an application of a terrestrial model coupled to an atmosphere-ocean general circulation model (AOGCM) has produced the same qualitative result [*Cox et al.*, 2000].

Here a complementary strategy is applied to investigate the climate-land biosphere feedbacks described above under the IPCC SRES nonintervention scenarios. Computationally efficient substitutes of the coupled European Center/Hamburg Model 3 and Large Scale Geostrophic (ECHAM3/LSG) AOGCM [*Voss et al.*, 1998; *Meyer et al.*, 1999; *Hooss et al.*, 2001; *Voss and Mikolajewicz*, 2001] and of the oceanic carbon cycle [*Siegenthaler and Joos*, 1992; *Joos et al.*, 1996] are coupled to the Lund-Potsdam-Jena Dynamic Global Vegetation Model (LPJ-DGVM) that simulates vegetation structure, carbon storage, and the water balance here at a resolution of $3.75^\circ \times 2.5^\circ$ [*Cramer et al.*, 2001; *Sitch*, 2000]. Adequately designed substitute models consist of a few equations only and require only a very modest amount of CPU time while yielding identical results for selected variables as the parent model [*Joos et al.*, 1996; *Huntingford and Cox*, 2000]. The use of substitute models combined with the computational efficiency of the LPJ-DGVM allows us to analyze a range of GHG emission scenarios and GHG concentration pathways, to run the model under alternative climate sensitivities, and to allow for alternative hypotheses, e.g., for the relationships between soil respiration and warming, or primary production and atmospheric CO_2. We are thus able to estimate the uncertainty in future terrestrial carbon storage and the associated uncertainty in projected CO_2, radiative forcing, and climate change.

This paper is organized as follows. In section 2 the coupled model and the SRES scenarios are described. In section 3, projected changes in radiative forcing and climate are presented for six illustrative SRES scenarios. Related changes in carbon storage and ecosystem structure are described. Next, we investigate carbon storage in response to changes in climate or changes in atmospheric CO_2 only and under different growth rates of radiative forcing and atmospheric CO_2. Before concluding, uncertainties in projected CO_2 and carbon storage and their impact on projected temperatures are estimated. Details of the model can be found in Appendix A.

2. Description of Model and Scenarios

2.1. Bern Carbon Cycle–Climate Model

The Bern carbon cycle-climate (Bern CC) model consists of a chemistry, radiative forcing, climate, and carbon cycle module (Figure 1). The model components are described in Appendix A and in the literature [*Prather et al.*, 2001; *Ramaswamy et al.*, 2001; *Hooss et al.*, 1999; *Voss and Mikolajewicz*, 1999; *Cubasch et al.*, 1997; *Voss et al.*, 1998; *Joos et al.*, 1996; *Siegenthaler and Joos*, 1992; *Cramer et al.*, 2001; *Sitch*, 2000; *Prentice et al.*, 2000; *McGuire et al.*, 2001]. The main features of the model are summarized below.

For scenario calculations, abundances of non-CO_2 GHGs are prescribed according to observations until 2000 and then calculated from SRES emissions. Calculating the abundance of chemically reactive gases from emissions requires a model that can predict how the lifetimes of these gases are changed by an evolving

atmospheric chemistry. Here we rely on results of a modeling workshop called OxComp where 14 state-of-the-art chemistry transport models were run under a set of emission scenarios. From the results of these simulations, simplified expressions were developed [*Prather et al.*, 2001; M. Prather, personal communication, September 2000] to estimate the evolution of OH and O_3 as a function of pollutant emissions and the impact of changing N_2O emissions on the lifetime of N_2O. Simplified expressions, lifetimes, and concentrations at year 2000 and at preindustrial time are given in Appendix A.

The radiative forcing [*Ramaswamy et al.*, 2001; *Shine et al.*, 1990; *Shine et al.*, 1994; *Shine and Forster*, 1999] from changes in the abundances of GHGs (CO_2, CH_4, N_2O, stratospheric and tropospheric O_3, stratospheric H_2O due to CH_4 changes, SF_6, and 28 halocarbons including those controlled by the Montreal Protocol), from direct and indirect effects of sulfate aerosols, and from direct forcing of black and organic carbon is calculated on the basis of simplified expressions [*Ramaswamy et al.*, 2001; *Harvey et al.*, 1996; *Myhre et al.*, 1998].

The model's climate component is an impulse response–empirical orthogonal function (IRF-EOF) substitute [*Hooss et al.*, 1999; *Hooss et al.*, 2001; *Voss and Mikolajewicz*, 1999; *Meyer et al.*, 1999] of the ECHAM3/LSG AOGCM [*Cubasch et al.*, 1997; *Voss et al.*, 1998], driven by radiative forcing. IRFs for perturbations in surface-air temperature, precipitation, cloud cover, and sea level rise characterize the adjustment time of the climate system to changes in radiative forcing, whereas EOFs describe the spatial patterns of the annual mean perturbations. The substitute was derived from a 850 year simulation with the ECHAM3/LSG model, wherein atmospheric CO_2 was quadrupled in the first 120 years and held constant thereafter [*Voss and Mikolajewicz*, 1999]. The climate sensitivities of the substitute for a doubling of atmospheric CO_2 corresponding to a change in radiative forcing of 3.7 W m^{-2} are 2.5°C (global mean surface-air temperature ΔT_{2x}), 64 mm yr^{-1} (global mean precipitation), −0.9% (cloud cover), and 128 cm (sea level) in the standard case. In sensitivity experiments, temperature sensitivities of 0°C (T0; constant climate) and 4.5°C (T45) [*Houghton et al.*, 1996] have been used; the sensitivities of other climate variables were scaled accordingly. This simple scaling tends to overestimate (underestimate) the transient temperature response for climate sensitivities higher (lower) than the ECHAM/LSG sensitivity as uptake of heat by the ocean is not explicitly simulated [*Hansen et al.*, 1984].

The carbon cycle component consists of a well-mixed atmosphere, the High-Latitude Exchange/Interior Diffusion-Advection (HILDA) ocean model [*Joos et al.*, 1996; *Siegenthaler and Joos*, 1992], and the LPJ-DGVM [*Cramer et al.*, 2001; *Sitch*, 2000; *Prentice et al.*, 2000; *McGuire et al.*, 2001]. The HILDA model and its substitute are used interchangeable and yield identical results. Surface to deep tracer transport in the ocean substitute is described by an IRF. The nonlinearities in air-sea gas exchange and carbon chemistry are captured by separate equations. The effect of sea surface warming on carbonate chemistry is included [*Joos et al.*, 1999b]. The LPJ-DGVM simulates the distribution of nine plant functional types (PFTs) based on bioclimatic limits for plant growth and regeneration and plant-specific parameters that govern plant competition for light and water. The PFTs considered are tropical broad-leafed evergreen trees, tropical broad-leafed raingreen trees, temperate needle-leaved evergreen trees, temperate broad-leaved evergreen trees, temperate broad-leaved summergreen trees, boreal needle-leaved evergreen trees, boreal summergreen trees, C_3 grasses/forbs, and C_4 grasses. Dispersal processes are not explicitly modeled, and an individual PFT can invade new regions if its bioclimatic limits and competition with other PFTs allow establishment. There are six carbon pools per PFT, representing leaves, sapwood, heartwood, fine roots, aboveground and belowground litter, and two soil carbon pools, which receive input from litter of all PFTs. Photosynthesis is modeled using a form of the Farquhar scheme [*Farquhar et al.*, 1980] with leaf-level optimized nitrogen allocation [*Haxeltine and Prentice*, 1996] and an empirical convective boundary layer parameterization [*Monteith*, 1995] to couple the carbon and water cycles. Decomposition rates of soil and litter organic carbon in the standard case depend on soil temperature [*Lloyd and Taylor*, 1994] and moisture [*Foley*, 1995]. Fire fluxes are calculated on the basis of litter moisture content, a fuel load threshold, and PFT specific fire resistances. The spatial resolution of the LPJ-DGVM is set to $3.75° \times 2.5°$. The LPJ-DGVM is spun up for 1000 years under preindustrial CO_2 and a baseline climate that includes interannual variability [*Cramer et al.*, 2001; *Leemans and Cramer*, 1991]. At year 400, soil carbon pool sizes are calculated analytically from annual litter inputs and annual mean decomposition rates. Spin-up is continued for another 600 years to reach equilibrium. For transient simulations the spatial fields in annual mean perturbations of temperature, cloud cover, and precipitation simulated by the ECHAM3/LSG substitute are added to the baseline climate. Test simulations suggest that the error in global carbon uptake arising from the IRF-EOF approach is 10%. LPJ was forced with the monthly fields of surface temperature, and precipitation was obtained with the ECHAM3/LSG for the "IPCC 1990 Business as Usual" scenario. Alternatively, the climate change pattern was represented by the first EOF of surface temperature and precipitation. Carbon uptake by 2084 is 543 and 607 Gt C for these two simulations. Deviations in local carbon uptake are generally <2 kg m^{-2}, and changes in vegetation structure are very similar in both simulations. Atmospheric CO_2 is prescribed until 1999 [*Etheridge et al.*, 1996; *Keeling and Whorf*, 1994], and the SRES carbon emissions are prescribed afterward. Land use changes are not explicitly considered in the present simulations because land use patterns for the SRES scenarios are not available. Instead, carbon fluxes from land use changes are prescribed externally according to the SRES scenarios. This approach probably tends to overestimate global terrestrial carbon storage as no attempt is made here to correct for the area that is not available for additional carbon storage due to land use.

The performance of the ECHAM3/LSG Model [*Cubasch et al.*, 1997; *Voss et al.*, 1998] has been evaluated in the framework of the Coupled Model Intercomparison Project (CMIP) [*Meehl et al.*, 2000; *Covey et al.*, 2000]. The LPJ-DGVM has been evaluated in combination with atmospheric transport models by comparing model results with the observed seasonal cycle in atmospheric CO_2 [*Sitch*, 2000] and its temporal trend [*McGuire et al.*, 2001] and by comparing the simulated time evolution and interannual variability of terrestrial carbon uptake with reconstructions based on atmospheric, CO_2, $\delta^{13}C$ and O_2:N_2 data [*McGuire et al.*, 2001]. The parameters of the box diffusion type ocean model were determined such that the model reproduces the observed oceanic distribution of natural and bomb-produced radiocarbon [*Siegenthaler and Joos*, 1992]; the model was evaluated with oceanic observations of ^{39}Ar and CFCs, and its parameterization for surface-to-deep transport was tested against the Geophysical Fluid Dynamics Laboratory (GFDL) Princeton ocean general circulation model [*Joos et al.*, 1997]. Model predictions for the decrease in atmospheric $\delta^{13}C$ and $\Delta^{14}C$ (Suess Effect) as well as the global budget of bomb-produced radiocarbon agree with observations within their error limits when the ocean is coupled to a box-type biosphere [*Joos and Bruno*, 1998]. Bern CC simulations of CO_2 uptake by ocean and land are within data-based reconstructions [*Battle et al.*, 2000; *Keeling et al.*, 1996; *Joos et al.*, 1999a]. Ocean uptake is 2.1 Gt C yr^{-1}, and biospheric uptake is 1.7 Gt C yr^{-1} for the period from 1980 to 1999. The combined model in its standard case simulates reasonably well the evolution of atmospheric CO_2

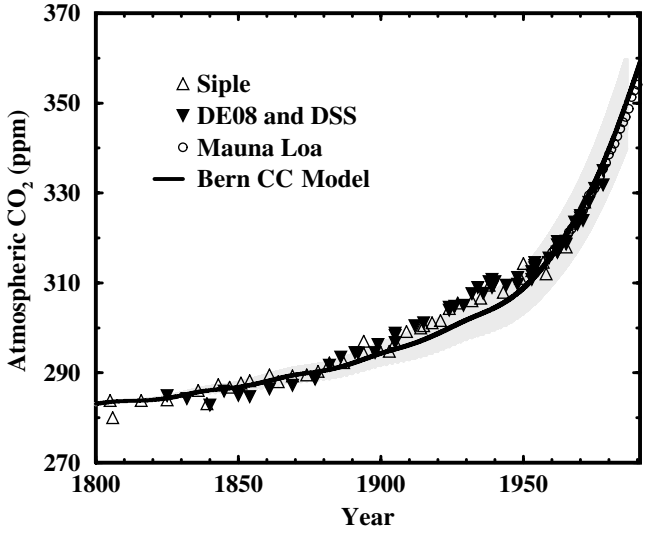

Figure 2. Observed versus simulated increase in atmospheric CO_2 during the industrial period. Data are from Antarctic ice cores drilled at Siple [*Neftel et al.*, 1985] and Law Dome (cores DE08 and DSS) [*Etheridge et al.*, 1996] and direct atmospheric observations at Mauna Loa, Hawaii [*Keeling and Whorf*, 1994]. The Bern CC model is forced by fossil [*Marland et al.*, 1995] and land use carbon emissions [*Houghton*, 1999] that are available until 1990. The shaded band was obtained by varying the emission data by ±1 standard deviation, taken to be 5% for fossil emissions and 31% for land use emissions.

during the industrial period (Figure 2) when driven by historical carbon emissions from fossil fuel burning, cement production, and land use [*Marland et al.*, 1995; *Houghton*, 1999]. The simulated increase in global average surface temperature since 1900 is 0.37°C, which is slightly lower than observed (0.6 ± 0.2°C) [*Folland et al.*, 2001].

2.2. SRES Emission Scenarios

The writing team of the Special Report on Emission Scenarios (SRES) of IPCC [*Nakićenović et al.*, 2000] has developed a set of emission scenarios for radiatively important gases up to 2100. There are four scenario "families" comprising a total of 40 scenarios. Each family includes several quantifications of a common narrative. None of the scenarios include any future policies that explicitly address climate change.

Here we analyze the six "illustrative marker scenarios" A1B, A1FI, A1T, A2, B1, and B2 taken to represent each family [*Nakićenović et al.*, 2000]. The A1 family describes a future with low population growth but rapid economic growth and high energy and material demands moderated by rapid technological change. The A1 scenario family develops into three groups that describe alternative directions of technology change in the energy system. The A1FI scenario is representative for a fossil-intensive energy sector; nonfossil energy sources are emphasized in the A1T scenario, whereas nonfossil energy sources and fossil sources are "balanced" in the A1B scenario. The A2 family describes a heterogeneous world with economic development regionally oriented, slow economic growth, and fast population growth. The B1 family describes a convergent world with low population growth as in A1 but with rapid changes in economic structure toward a service and information economy and the introduction of clean technologies. The B2 family describes a world in which the emphasis is on local solutions, with moderate population growth, intermediate levels of economic development, and less rapid technological change than in A1 or B1.

3. Results

3.1. Changes in Radiative Forcing and Climate

First, we evaluate climatic consequences of the six marker scenarios for the standard model setup. Cumulative carbon emissions between 2000 and 2100 range between 690 and 2455 Gt C for all 40 SRES scenarios. The range of the six analyzed marker scenarios is somewhat narrower: 981 Gt C (B1) to 2107 GtC (A1FI) (Figure 3a). Atmospheric CO_2 is projected to increase from 367 ppm at the beginning of year 2000 to 540 ppm at year 2100 for the lowest (B1) and to 958 ppm for the highest emission scenario (A1FI) (Figure 3b), corresponding to an increase in radiative forcing of 2.1 and 5.1 W m^{-2} respectively.

Radiative forcing by non-CO_2 GHGs is 1.3 W m^{-2} at 2000 and is projected to be between 1.2 (B1) and 3.3 W m^{-2} (A1FI and A2) at year 2100. However, radiative forcing by all non-CO_2 agents is estimated to be close to zero during the twentieth century because the negative forcing by aerosols approximately cancels the positive forcing by non-CO_2 GHGs (Figure 3c) in our model configuration. Projected radiative forcing by all agents is intermediate during the next three decades for the most carbon-intensive scenarios because the effect of high carbon emissions from coal burning is partly masked by concomitant high sulfur emissions (Figure 3c). We emphasize that the magnitude of the aerosol forcing is highly uncertain [*Houghton et al.*, 1996; *Shine and Forster*, 1999]. However, the relative importance of aerosol-induced cooling decreases under the six marker scenarios because it is assumed that sulfur emission controls are strengthened. Radiative forcing by sulfate aerosols is estimated to be −1.2 W m^{-2} at 2000 and between −1.1 W m^{-2} (A2) and −0.4 W m^{-2} (A1T) at 2100. Changes in radiative forcing by organic and black carbon aerosols are estimated to be small (−0.16 to +0.05 W m^{-2}). Taken together, we estimate an increase in radiative forcing between 2000 and 2100 of 0.0 W m^{-2} (A2) to +0.7 W m^{-2} (B1) from changes in aerosols. This is relatively small compared to the range for total radiative forcing of 2.8 W m^{-2} (B1) to 7.5 W m^{-2} (A1FI).

Global average surface-air temperature is modeled to increase by 0.5°C up to 2000 and a further 1.6°C (B1) to 3.5°C (A1FI) up to 2100 (Figure 3d). The simulated temperature increase is largest in high northern latitudes and in continental regions, 4°–6°C in North America and Eurasia for scenario A1B at year 2100 (Plate 1a). For scenario A1B and year 2100, precipitation changes are between −40 and +60 cm yr^{-1} (Plate 1b). Projected ocean thermal expansion is between 19 and 30 cm (Figure 3e). In conclusion, atmospheric CO_2, radiative forcing, temperature, and ocean thermal expansion continue to increase for all six scenarios.

3.2. Changes in Terrestrial Carbon Storage and Ecosystem Structure

For simplicity, we restrict discussion of the role of terrestrial ecosystem changes to scenario A1B and note that results are qualitatively similar for the other five SRES scenarios. Results of various sensitivity experiments are summarized in Table 1. In the standard experiment T25 (ΔT_{2x} = 2.5°C), global terrestrial carbon sequestration for scenario A1B is between 2 and 3 Gt C yr^{-1} during the 21st century (Figure 4a). Soils and vegetation in tropical areas and high northern latitudes are carbon sinks, whereas soils and vegetation in northern midlatitude regions become carbon sources (Plate 2a). Simulated ecosystem changes are substantial (Plate 2b). Tree coverage by tropical raingreen and evergreen trees is enhanced in the tropics and subtropics, in contrast to *Cox et al.* [2000], as soil moisture is increased. Boreal trees are partly replaced by temperate deciduous trees or grasses due to warmer

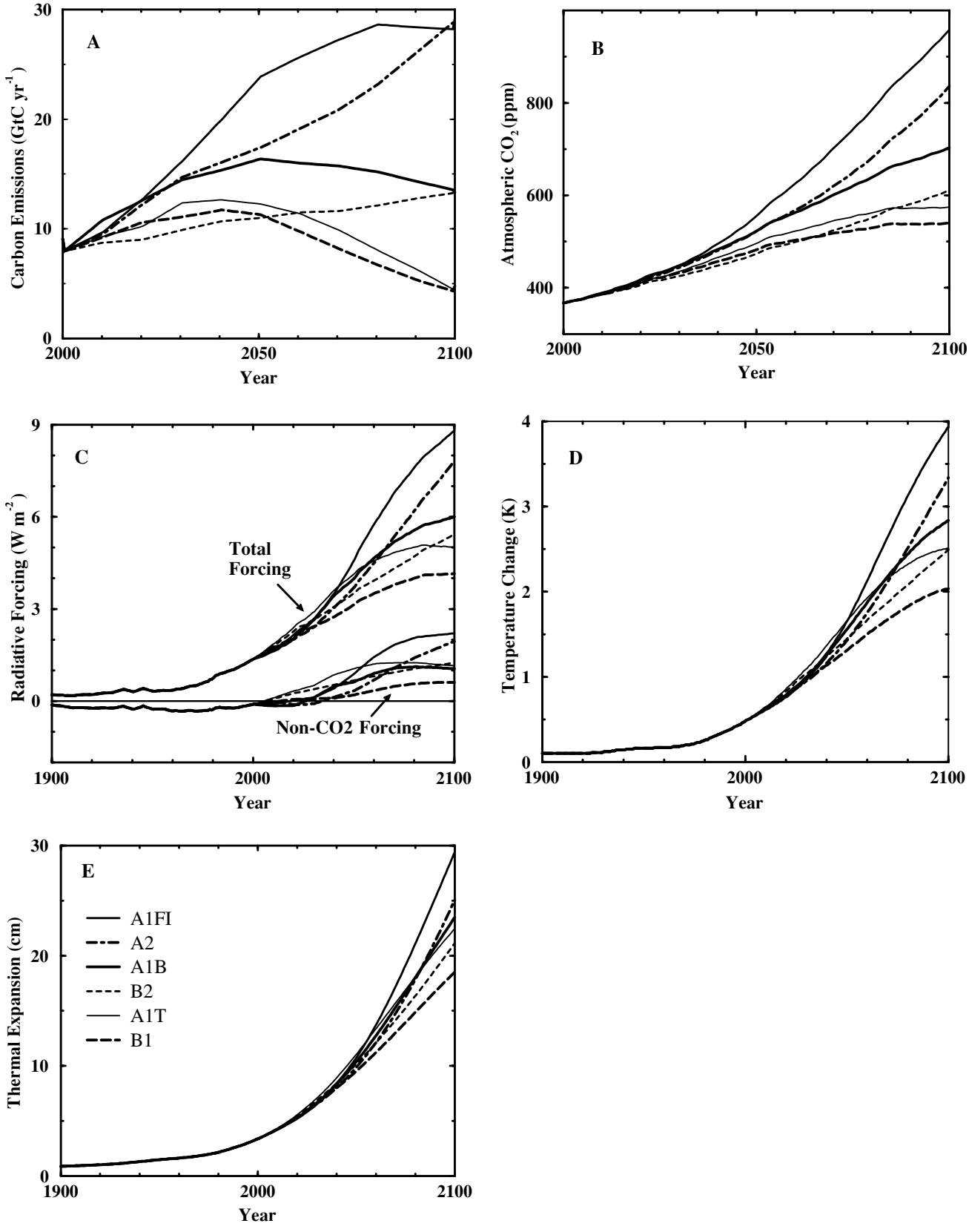

Figure 3. (a) Prescribed anthropogenic carbon emissions and projected (b) atmospheric CO_2, (c) radiative forcing by all agents and all non-CO_2 agents, (d) change in global average surface temperature, and (e) ocean thermal expansion for the SRES illustrative marker scenarios A1B, A2, B1, B2, A1FI, and A1T. The model's climate sensitivity is set to 2.5°C.

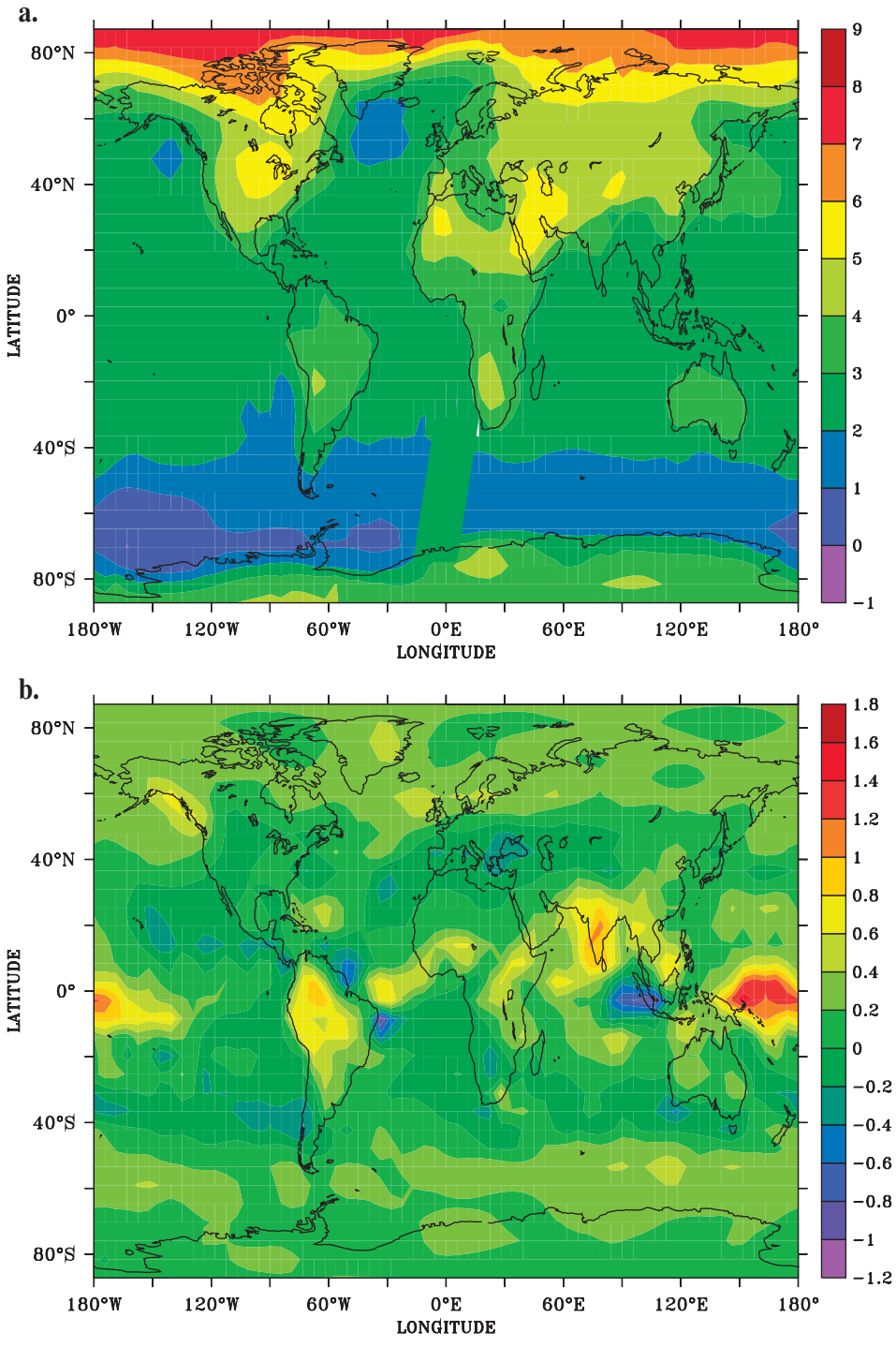

Plate 1. Simulated distribution of (a) annual mean surface warming and (b) precipitation changes since preindustrial time at year 2100 for scenario A1B. Surface warming is in °C; precipitation changes are in mm day^{-1}. The model's climate sensitivity is set to 2.5°C.

winters favoring temperate trees, while hot summers reduce the viability of boreal trees. These changes reduce the total forested area by 1.5×10^{12} m^2 between 40° and 60°N. The warming in high northern latitudes leads to a progressive poleward spread of boreal trees in North America and Siberia. Tree coverage north of 60°N is enhanced by 2.7×10^{12} m^2. These simulated ecosystem changes are comparable with paleodata showing more extensive distribution of temperate deciduous forests and grasslands in the continental interior, together with a northward shift of the boreal tree line in response to warming of comparable magnitude in northern middle to high latitudes during the mid-Holocene [*COHMAP Members*, 1988; *Prentice et al.*, 1991]. However, projected future changes cannot be directly compared with Holocene changes as climatic changes progressed much slower during the

Table 1. Model Results for Scenario A1B

Simulation	Description	CO_2 in 2100, ppm	Carbon Uptake 2000–2099, Gt C		Mean Surface Warming 1765–2100, °C
			Land	Ocean	
C-slow	CO_2 fertilization capped at year 2000; slow ocean	918	−147	390	3.5
C	CO_2 fertilization capped at year 2000	856	−130	505	3.3
T45	climate sensitivity increased ($\Delta T_{2\times}$ = 4.5°C)	805	52	432	5.6
T25	standard model setup ($\Delta T_{2\times}$ = 2.5°C)	703	282	418	2.8
T0	no climate change ($\Delta T_{2\times}$ = 0.0°C)	632	438	415	0.0
R	soil and litter respiration rates do not depend on global warming	636	470	374	2.6
R-fast	soil and litter respiration rates do not depend on global warming; fast Ocean	617	449	433	2.5

Holocene than the changes projected for the 21st century and because the nature of the forcing was different (i.e., orbital variations as opposed to greenhouse gas variations). Nevertheless, the paleodata indicate that the projected trends of vegetation response are consistent with regional changes in vegetation structure that have occurred in the geologically recent past.

The climate sensitivity of the ECHAM3/LSG model is at the lower end of the current set of coupled AOGCMs. In experiment T45 the climate sensitivity is increased to 4.5°C. The dieback of boreal trees is then greater, and soil and litter turnover rates are increased. The carbon loss in the boreal and temperate zone becomes larger than the carbon gain in the tropics and high northern latitudes, so that the terrestrial biosphere turns into a carbon source for all six SRES scenarios considered (Figure 4a).

3.3. Changes in Carbon Storage in Response to Changes in CO_2 or Climate Only

We present two sensitivity experiments, C0 and T0, to further analyze the pattern of terrestrial carbon sources and sinks. In T0 the model's climate sensitivity is set to zero. Then, CO_2 changes are the only driving force for terrestrial carbon storage. Terrestrial carbon uptake then increases to 4 Gt C yr^{-1} in the second half of the century (Figure 4a). The modeled CO_2 fertilization mechanism is especially effective in tropical forests because of their high NPP, high photorespiration rates (which are reduced in high CO_2), and long timescales for turnover of vegetation carbon (Plate 3a). Ecosystem structure changes are relatively small. Tropical evergreen tree cover is slightly increased, and trees invade arid regions, in part because of increased water use efficiency accompanied by an only modest increase in carbon release by fires and in part because of more effective competition of tree seedlings (with the C_3 photosynthetic pathway) against the dominant C_4 grasses in tropical savannas. The effects of phosphorus limitations and land use pressure which may be large in tropical regions are not considered in the model.

CO_2 fertilization is shut off in experiment C0 by keeping CO_2 in the model's photosynthesis module at preindustrial level, so that only climate change affects terrestrial carbon storage. The terrestrial biosphere then releases carbon, as a consequence of increased soil and litter respiration rates under the simulated warmer and slightly more humid conditions, except in cold climates where growing season length strongly increases (Plate 3b). Forest dieback in limited regions of the northern continental interior leads to a loss of >12 kg C m^{-2} from the boreal zone by 2100. The climate and CO_2 fertilization mechanisms are not additive; their synergistic effects lead to higher carbon storage in T25 than for the sum of C0 and T0. Similarly, the reduction in tree cover in midlatitude regions is smaller, and the stimulation of tree growth in the high north is larger in T25. Experiments C0 and T0 illustrate that global terrestrial carbon uptake or release represents a balance between carbon gain by CO_2 fertilization and vegetation increase mainly in high-latitude and high-altitude regions and carbon loss due to generally increased soil respiration rates, compounded by forest dieback in some boreal regions. This balance may change over time, as illustrated in section 3.4.

3.4. Carbon Storage and Growth Rates in Radiative Forcing and CO_2

We investigated how the magnitude of the terrestrial sink/source may depend on the rate of increase of atmospheric CO_2 and radiative forcing. Atmospheric CO_2 was prescribed to increase exponentially to 1000 ppm within 70 or 210 years and stabilized thereafter (Figure 5a). Non-CO_2 radiative forcing was set to zero or to 25% of the radiative forcing by CO_2 and $\Delta T_{2\times}$ was set to 4.5°C. Simulations were continued from the end of the spin-up at model year 1000 until model year 2000 when a new equilibrium is approached. The terrestrial biosphere becomes a CO_2 source for several decades either when atmospheric CO_2 increases rapidly or when non-CO_2 radiative forcing is large (Figure 5b). In this case, the carbon loss due to climate change dominates for a few decades over the carbon gain by CO_2 fertilization. At the new equilibrium, carbon storage has increased by 400 Gt C when non-CO_2 radiative forcing is set to zero but only by 110 Gt C when non-CO_2 radiative forcing is 25% of the radiative forcing by CO_2. Cumulative ocean uptake until model year 2000 is 2100 and 1990 Gt C for the two cases and the fast atmospheric CO_2 pathway. These findings imply that the emission rate of non-CO_2 GHGs affects the growth rate of atmospheric CO_2. High rates of GHG emissions and high contributions of non-CO_2 gases to the total radiative forcing could lead to reduced terrestrial carbon storage (or even to a terrestrial carbon source) during this century.

The evolution in simulated carbon storage reflects the different timescales associated with the governing processes. The relevant processes are enhanced productivity and water use efficiency with increasing CO_2 (CO_2 fertilization), loss of soil and litter carbon due to increasing respiration rates, and local dieback of boreal trees and their replacement by temperate trees or grasses under rising temperatures. Figure 5c shows the evolution of primary productivity and the carbon stored globally in vegetation and in soils (including litter) and of global average surface temperature for the experiment where atmospheric CO_2 reaches 1000 ppm within 70 years and non-CO_2 radiative forcing is 25% of the radiative forcing

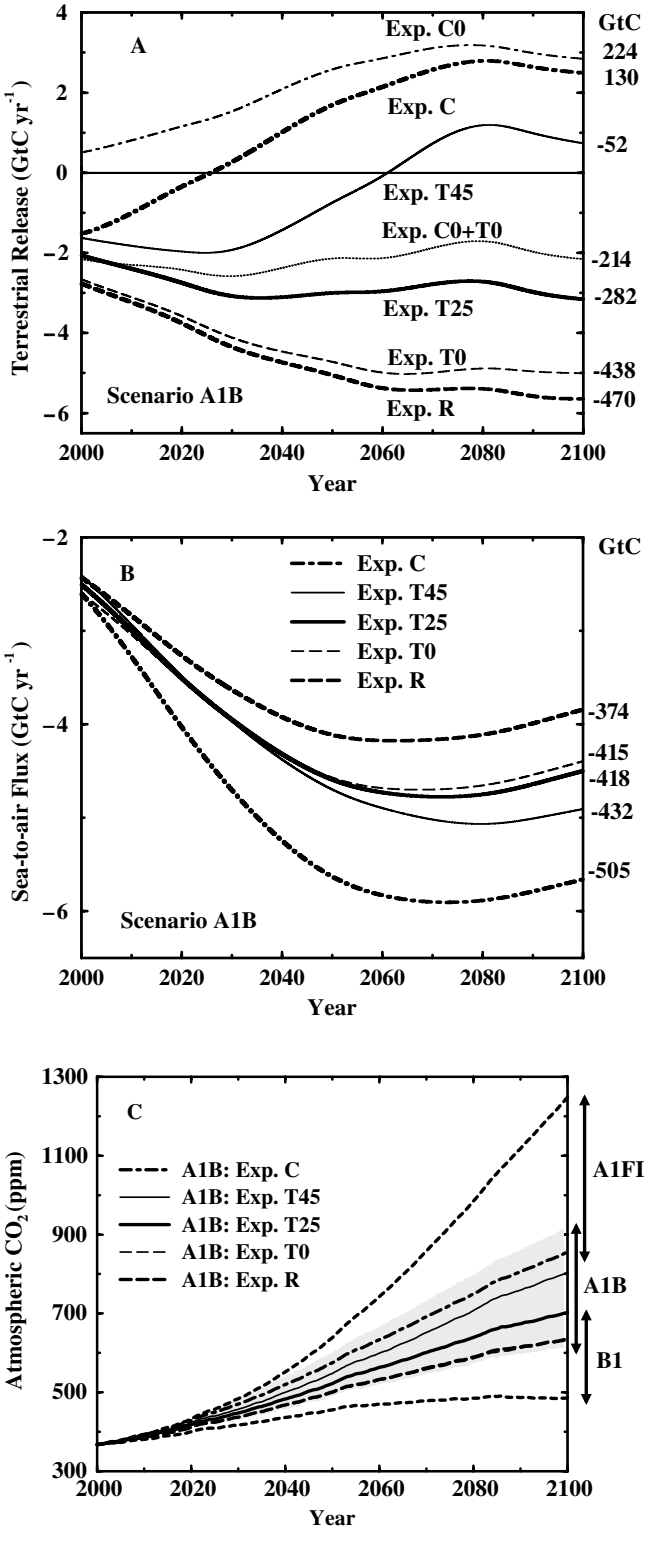

by CO_2. The increase in surface temperature lags the increase in atmospheric CO_2 (Figure 5) due to the thermal inertia of the ocean. Primary productivity increases about linearly in the first 80 years of the simulation and stabilizes soon after atmospheric CO_2 has been stabilized. Carbon storage in vegetation increases because of rising productivity during the first 50 years; then, uptake is stalled during the next few decades as the carbon gain by enhanced productivity is compensated by carbon loss due to dieback of boreal trees. Temperate trees invade the boreal zone within the following decades, and carbon storage in vegetation increases toward a new equilibrium. Carbon storage in soil increases during the first few decades as input from vegetation outweighs loss by increasing soil respiration rates. At higher temperatures, soil carbon is lost to the atmosphere. The whole terrestrial biosphere acts as a carbon source around the time of CO_2 stabilization (Figure 5), when temperatures and soil respiration reach high levels while soil and litter pools are still large. The biosphere is also a source of carbon during the centuries after model year 1400, as carbon storage in vegetation approaches equilibrium while soil carbon continues to be lost to the atmosphere due to the long adjustment time of the soil reservoir.

3.5. Uncertainties in Projected CO_2 and Carbon Storage

We also investigated the consequences of alternative (extreme) model assumptions about terrestrial ecosystem processes. First, the extent of stimulation of carbon storage in natural ecosystems by CO_2 has been a matter of controversy [*Hättenschwiler et al.*, 1997; *Luo et al.*, 1999]. There is no proof that the biospheric sink on the global scale is indeed primarily due to CO_2 fertilization, as would be implied by the LPJ-DGVM results. Other process, such as nitrogen fertilization [*Schindler and Bayley*, 1993; *Townsend et al.*, 1996], climate variations [*McGuire et al.*, 2001; *Dai and Fung*, 1993], and forest regrowth [*Dixon et al.*, 1994; *Caspersen et al.*, 2000], might in principle be responsible for part or most of the terrestrial sink. If this were the case, then it would be unlikely that primary productivity would increase as a function of future CO_2 concentrations. A simple alternative hypothesis is that primary productivity remains close to its present level. In experiment C, CO_2 fertilization is capped after year 2000; this is achieved by keeping CO_2 constant at the concentration of year 2000 in the photosynthesis routine. Modeled carbon uptake by CO_2 fertilization until year 2000 is thus taken as a surrogate for an unknown process (in order to balance the present global budget), and it is assumed that this unknown sink process has just reached saturation. Then, the terrestrial biosphere turns into a source within the next two decades and around 130 Gt C are released by the end of the century (Figure 4a). Second, there is conflicting evidence on the temperature dependence of soil and litter respiration [*Trumbore et al.*, 1996; *Giardina and Ryan*, 2000; *Jarvis and Linder*, 2000; *Rustad*, 2000] over multiannual timescales. A recent synthesis [*Rustad*, 2000] of results of 32

Figure 4. Sensitivity tests on (a) projected terrestrial carbon release, (b) sea-to-air flux, and (c) atmospheric CO_2 under scenario A1B. Cumulative carbon release for 2000–2100 is given in Gt C at the right; negative numbers denote terrestrial uptake in Figure 4a. In T0, T25, and T45 the climate sensitivity $\Delta T_{2\times}$ of the ECHAM3/LSG substitute is varied between 0° (constant climate), 2.5° (standard case), and 4.5°C. In R, soil respiration does not depend on global warming. In C0, CO_2 fertilization is shut off, and in C, CO_2 fertilization is capped after year 2000. $\Delta T_{2\times}$ is 2.5°C in experiments C0, C, and R. The terrestrial model setup of experiment C is combined with a slow overturning version of the ocean model, and the terrestrial setup of experiment R is combined with a fast overturning ocean to yield upper and lower estimates in projected CO_2 (shaded area in Figure 4c). The upper limit (R-fast) for scenario A1FI and the lower limit (R-slow) for scenario B1 is shown by thick dashed lines. The arrows show the ranges (R-fast to C-slow) in projected CO_2 for scenarios A1B, B1, and A1FI at year 2100. Interannual variability in terrestrial release and in sea-to-air fluxes has been removed by a smoothing spline.

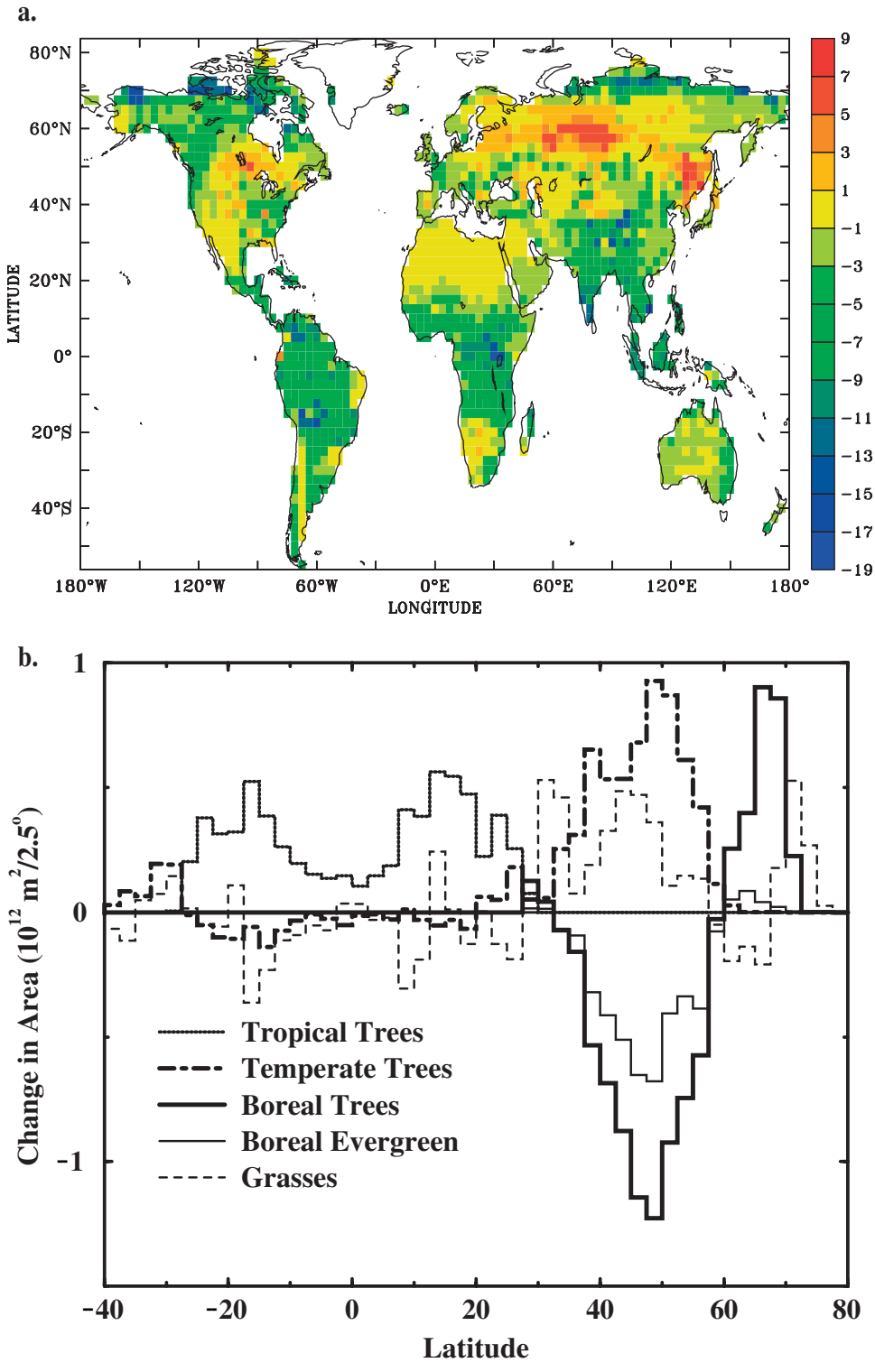

Plate 2. Simulated changes up to 2100 in (a) terrestrial carbon storage in kg C m^{-2} (negative numbers denote uptake) and (b) the area covered by grass and tropical, temperate, and boreal trees per 2.5° latitudinal zone for scenario A1B, standard experiment (T25).

ecosystem warming experiments with duration between 2 and 9 years in different biomes shows that soil respiration rates increase in general with warming, but the change in respiration rate is found to be small (or even negative) at some sites. In experiment R, soil and litter respiration rates are assumed to be independent of global warming [*Giardina and Ryan*, 2000]. Global carbon storage is then increased by 188 Gt C, relative to experiment T25, by 2100 (Figure 4a).

Finally, we explore the impact of uncertainties in the oceanic and terrestrial response on projected CO_2 and climate. Experi-

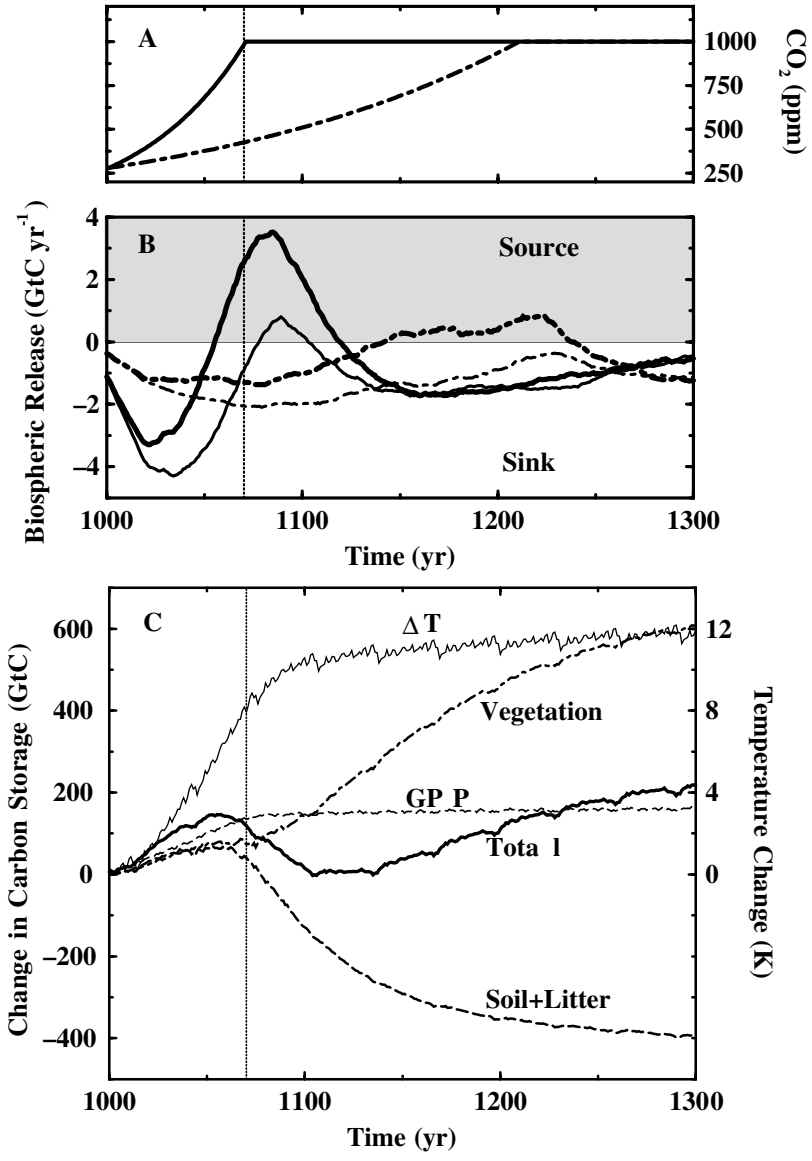

Figure 5. (a) Atmospheric CO_2 is prescribed in transient simulations to increase exponentially within 70 and 210 years to a level of 1000 ppm and kept constant afterward. (b) Terrestrial carbon release simulated when prescribing CO_2 profiles shown in Figure 5a. Non-CO_2 radiative forcing is set to zero (thin line) or to 25% of the CO_2 radiative forcing (thick line). The model's climate sensitivity $\Delta T_{2\times}$ is set to 4.5°C. Interannual variability in terrestrial release has been removed by smoothing. (c) Evolution of globally averaged surface temperature (thin solid line), carbon storage in vegetation (thick dot-dashed line), carbon storage in litter and soil (thick dashed line), and total biospheric storage (thick solid line). The increase in gross primary productivity is given in Gt C yr^{-1} (thin dashed line; left axis). The transient simulation started at the end of the spin-up at model year 1000, and time is given in years since the start of the spin-up.

ments R and C represent upper and lower estimates for terrestrial carbon storage. The difference in the cumulative carbon uptake during this century amounts to 600 Gt C. This would correspond to a difference in projected CO_2 of 283 ppm (1 ppm = 2.123 Gt C). However, the ocean absorbs 131 Gt C more between year 2000 and 2100 under experiment C than under experiment R (Figure 4b) because of the higher growth in atmospheric CO_2 in experiment C. Thus 20% of the difference in terrestrial storage is counteracted by the ocean response, and the difference in projected CO_2 is accordingly reduced. Data-based estimates yield an average oceanic uptake of 2 ± 0.6 Gt C yr^{-1} for the 1980s. We have scaled all transport parameters of the ocean model (including gas exchange) by a factor of 0.5 and 1.5, thereby mimicking a faster and slower overturning ocean. Average ocean uptake for the period from year 1980 to 1989 is 2.0 Gt C yr^{-1} for the standard model setup, 1.46 Gt C yr^{-1} for the "slow ocean," and 2.54 Gt C yr^{-1} for the "fast ocean" in accordance with the range of data-based estimates. Cumulative ocean uptake during the century is ±90 Gt C, roughly 20% different compared to the standard ocean model setup for scenario A1B. Combining the fast overturning ocean and the terrestrial model setup of experiment R (experiment R-fast) yields a lower limit in projected CO_2, while combining the slow overturning ocean with experiment C (experiment C-slow) yields an upper limit. For scenario A1B, projected CO_2 is 620 and 920 ppm at year 2100 for the two experiments. Projected CO_2 varies between 820 and 1250 ppm for scenario A1FI and between 490 and 680 ppm for scenario B1 (Figure 4c). This

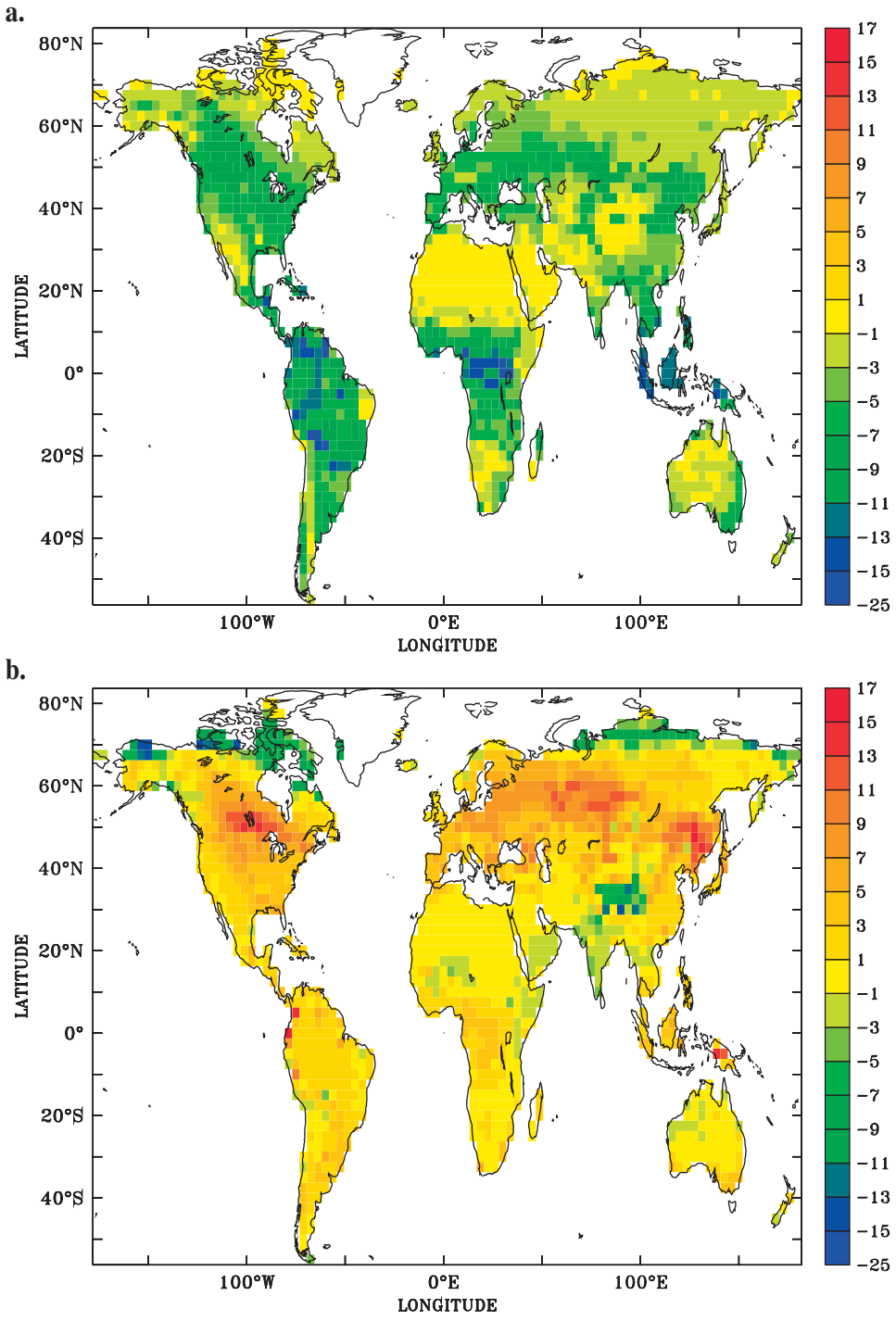

Plate 3. Simulated changes up to 2100 in terrestrial carbon storage in kg C m^{-2} (negative numbers denote uptake) for scenario A1B and experiment (a) T0, where the models climate sensitivity is set to zero (no climate change), and (b) for experiment C0, where CO_2 fertilization is suppressed.

translates into a deviation in global average surface temperature at year 2100 of roughly −0.3° to +0.6°C compared to that of the standard A1B, A1FI, and B1 simulations. The range in projected CO_2 is smaller than the sum of the uncertainty ranges in terrestrial and oceanic storage. This is because uncertainties in oceanic uptake are moderated through changes in terrestrial uptake and vice versa. In conclusion, the above analyses suggest that for a given emission scenario, projected CO_2 at 2100 is uncertain by −10 to +30% because of uncertainties in modeled land and ocean processes.

4. Discussion and Conclusion

Limitations of our modeling studies are that land use changes are not explicitly considered and that modeled land surface changes do

not affect the circulation and the hydrological cycle in the atmosphere. Regional model results need to be interpreted with caution also because different climate models yield different regional changes in temperature and precipitation, which could imply important differences in the response of the terrestrial biosphere to global climate change.

For a range of model assumptions, we find that the terrestrial biosphere could act as a strong carbon source or sink during this century. Factors that influence terrestrial carbon storage are the assumed sensitivity of climate to radiative forcing [*Houghton et al.*, 1996], the sensitivity of soil respiration to temperature [*Giardina and Ryan*, 2000; *Lloyd and Taylor*, 1994], and the rate of increase in radiative forcing by both CO_2 and other GHGs. For a given emission scenario, projected atmospheric CO_2 is estimated to be uncertain by -10 to +30%. From these results and from earlier studies investigating feedbacks on oceanic carbon uptake [*Maier-Reimer et al.*, 1996; *Sarmiento and Le Quéré*, 1996; *Matear and Hirst*, 1999; *Joos et al.*, 1999b; *Plattner et al.*, 2001], we conclude that uncertainties in our understanding of basic mechanisms have a significant impact on projected CO_2 and climate. Nevertheless, the difference among the SRES scenarios are large, and it is clear that anthropogenic carbon emissions themselves will represent the dominant control over atmospheric CO_2 concentration during the next 100 years.

Cox et al. [2000] applied version HadCM3 of the Hadley Centre climate model coupled to a carbon cycle model for scenario IS92a. They projected atmospheric CO_2 to rise to 980 ppm by 2100. For the same scenario and year the Bern CC model yields 700 ppm (range of 630–900 ppm). The difference in simulated CO_2 concentration is due in part to a much slower surface to deep water transport in the Hadley Centre model than in the Bern CC model and in part to the representation of soil and litter carbon by one single reservoir in combination with a high simulated warming rate, which causes a substantial fraction of this carbon to be rapidly released. In comparison with observations, the atmospheric CO_2 increase up to 2000 is overestimated by 15%, and the increase in global mean surface temperature is overestimated by more than a factor of 2 in the simulation by *Cox et al.* [2000]. The high simulated warming rate is due to the neglect of cooling by sulphate aerosols, and the relatively high climate sensitivity of HadCM3. When combined with a conventional formulation of the dependence of soil respiration rates on temperature, the high warming rate results in a massive loss of carbon from soil and litter. Current ocean carbon uptake in HadCM3 is at the lower end of both data-based estimates and the range of current three-dimensional ocean models, suggesting that the simulated surface to deep water mixing rate may be too sluggish. In simulations where CO_2 reaches around 700 ppm at 2100, ocean uptake for the period from 2000 to 2100 is 410 Gt C in the Bern CC model but only 250 Gt C in the Hadley Centre model.

Shifts in ecosystem structure are found for all six illustrative nonintervention scenarios in the Bern CC model. Boreal trees in middle northern latitudes are replaced to a greater or lesser extent by grasses and temperate trees, whereas boreal trees invade high northern latitudes. Paleodata confirm that analogous vegetation changes have taken place (albeit in response to much slower climate changes) as those simulated for the next hundred years, and comparably rapid changes in vegetation structure are known to have occurred earlier during rapid climate change episodes, such as beginning and end of the Younger Dryas cold event [e.g., *Cooperative Holocene Mapping Project Members*, 1988; *Birks and Ammann*, 2000]. Such changes taking place in the modern world would inevitably impact regional forest industries and economies. The extent of the regions affected depends on the magnitude of the climate change, which in turn depends on GHG emissions.

High GHG emissions and a high contribution of non-CO_2 agents to radiative forcing tend to reduce the fraction of the anthropogenic carbon emissions that is taken up by the terrestrial biosphere and the ocean. For example, 57% of the anthropogenic emissions are still airborne at 2100 for scenario A1FI, whereas only 41% remain airborne for scenario B1. This suggests that low GHG emissions yield a double dividend, allowing a lower rate of warming and a lower fraction of CO_2 emissions remaining in the atmosphere.

Appendix A

A1. Abundances and Burdens of Non-CO_2 Greenhouse Gases

Calculating the abundance of chemically reactive gases from emissions requires a model that can predict how the lifetimes of these gases are changed by an evolving atmospheric chemistry. Here we rely on results of a modeling workshop called OxComp where 14 state-of-the-art chemistry transport models were run under a set of emission scenarios. From the results of these simulations, simplified expressions were developed to estimate the evolution of OH and O_3 as a function of pollutant emissions and the impact of changing N_2O emissions on the lifetime of N_2O as summarized below [*Prather et al.*, 2001; M. Prather, personal communication, September 2000].

Global mean atmospheric abundances or burdens are projected using anthropogenic emissions from *Nakićenović et al.* [2000]. Changes in CH_4, N_2O, the fully fluorinated species SF_6, CF_4, C_2F_6, C_4F_{10}, and the halocarbons HFC-23, HFC-32, HFC-125, HFC-134a, HFC-143a, HFC-152a, HFC-227ea, HFC-245ca, and HFC-43-10mee are estimated from the budget equation:

$$\frac{dC}{dt} = E - \frac{1}{\tau}C, \tag{A1}$$

where C is the concentration (in ppb), E is total (natural and anthropogenic) emission (in ppb yr^{-1}), and τ is the lifetime (in years).

Natural emissions for CH_4 and N_2O are estimated from (A1) by specifying all other terms for today. For CH_4 the present lifetime is taken to be 8.4 years, the concentration is taken to be 760 ppb, corresponding to a burden of 4885 Tg(CH_4), the atmospheric increase is taken to be 22 Tg(CH_4) yr^{-1}, and anthropogenic emissions are 323 Tg(CH_4) [*Prather et al.*, 2001; *Nakićenović et al.*, 2000]. This yields a natural flux to the atmosphere of 301 Tg(CH_4). For N_2O the present lifetime is taken to be 120 years, the concentration is taken to be 316 ppb, corresponding to a burden of 1520 Tg N, the atmospheric increase is taken to be 3.8 Tg N yr^{-1}, and anthropogenic emissions are 7.0 Tg N [*Nakićenović et al.*, 2000]. This yields a natural flux to the atmosphere of 9.5 Tg N [*Prather et al.*, 2001].

The lifetime of N_2O is estimated taking into account the effect of a changing N_2O burden on its own life time by

$$\tau(\mathrm{N_2O}) = 120 \text{ years} \left(\frac{e\mathrm{N_2O}(t)}{e\mathrm{N_2O}(2000)} \right)^{-0.055}, \tag{A2}$$

where eN$_2$O are total N_2O emissions (in Tg N yr^{-1}).

The relative change in tropospheric OH with respect to year 2000, rOH, is used to scale lifetimes of greenhouse gases reacting with OH. It is estimated by

$$\begin{aligned} \ln(r\,\mathrm{OH}) = \ln\frac{\mathrm{OH}(t)}{\mathrm{OH}(2000)} &= -0.32 \ln\left(\mathrm{CH_4}(t)/\mathrm{CH_4}(2000)\right) \\ &+0.0042(e\mathrm{NO}_x(t) - e\mathrm{NO}_x(2000)) \\ &-0.000105(e\mathrm{CO}(t) - e\mathrm{CO}(2000)) \\ &-0.000315(e\mathrm{VOC}(t) - e\mathrm{VOC}(2000)), \end{aligned} \tag{A3}$$

where CH_4 is atmospheric methane (in ppb), eNO_x denotes anthropogenic NO_x emissions in Tg N yr^{-1}, and eCO and eVOC are anthropogenic emissions of CO and volatile organic carbon compounds, respectively (in Tg yr^{-1}).

The lifetime τ of CH_4 is then estimated from the present lifetimes with respect to reaction with OH (9.6 years), destruction in the stratosphere (120 years) and in soils (160 years), and the changes in OH:

$$\frac{1}{\tau(\mathrm{CH_4})} = \frac{r\ \mathrm{OH}}{9.58\ \mathrm{years}} + \frac{1}{68.2\ \mathrm{years}} \tag{A4}$$

The lifetimes of the fully fluorinated species (SF_6, CF_4, C_2F_6, and C_4F_{10}) are taken as time invariant, whereas the lifetimes of other halocarbons are scaled with OH:

$$\tau(t) = \frac{\tau(2000)}{r\ \mathrm{OH}} \tag{A5}$$

Tropospheric O_3 (in Dobson units (DU)) is estimated from

$$\begin{aligned}\mathrm{O_3}(t) = \mathrm{O_3}(2000) &+ 5.0\ \ln\left[\mathrm{CH_4}(t)/\mathrm{CH_4}(2000)\right] \\ &+ 0.125\left[e\mathrm{NO}_x(t) - eNO_x(2000)\right] \\ &+ 0.0011\left[e\mathrm{CO}(t) - e\mathrm{CO}(2000)\right] \\ &+ 0.0033\left[e\mathrm{VOC}(t) - e\mathrm{VOC}(2000)\right].\end{aligned} \tag{A6}$$

CH_4 denotes atmospheric methane, eNO_x is anthropogenic emissions of NO_x (in Tg N yr^{-1}), eCO and eVOC are anthropogenic emissions of CO and VOC (in Tg yr^{-1}). The coefficients in the above equation represent recently updated values (M. Prather, personal communication, April 2001), whereas ~25% larger coefficients (6.7, 0.17, 0.0014, and 0.0042) were used in this study.

Lifetimes and concentrations at year 2000 and at preindustrial time t_0 are given in Table A1. Concentrations of species controlled under the Montreal Protocol are not calculated but are prescribed following United Nations Environment Programme (UNEP)/World Meteorological Organization (WMO) Scientific Assessment of Ozone Depletion [*UNEP/WMO*, 1998].

A2. Radiative Forcing by Greenhouse Gases

Radiative forcing provides a convenient first-order measure of the climatic importance of perturbations to the planetary radiation balance [*Ramaswamy et al.*, 2001; *Shine et al.*, 1990; *Shine and Forster*, 1999]. Global radiative forcing (RF) by well-mixed greenhouse gases is well defined (±10%), whereas present and future radiative forcing by changes in tropospheric and stratospheric ozone are much more uncertain (approximately factor 2) [*Shine and Forster*, 1999]. Here radiative forcing is estimated from projected abundances using published simplified expressions [*Ramaswamy et al.*, 2001; *Myhre et al.*, 1998; *Harvey et al.*, 1996].

Radiative forcing for CO_2 is

$$\mathrm{RF}(\mathrm{CO_2}) = 5.35\ \mathrm{W\ m^{-2}} \left(\ln \frac{\mathrm{CO_2}(t)}{\mathrm{CO_2}(t_0)} \right), \tag{A7}$$

where t_0 is the preindustrial reference time. Radiative forcing for CH_4 (in ppb) is

$$\begin{aligned}\mathrm{RF}(\mathrm{CH_4}) = 0.036\ \mathrm{W\ m^{-2}} &\left[\sqrt{\mathrm{CH_4}(t)} - \sqrt{\mathrm{CH_4}(t_0)} \right] \\ &- f[\mathrm{CH_4}(t), \mathrm{N_2O}(t_0)] - f[\mathrm{CH_4}(t_0), \mathrm{N_2O}(t_0)].\end{aligned} \tag{A8}$$

The function f that accounts for the overlap in CH_4 and N_2O (in ppb) bands is

$$\begin{aligned}f(M,N) = &\ 0.47 \\ &\cdot \ln\left(1 + 2.01 \times 10^{-5}(MN)^{0.75} + 5.31 \times 10^{-15} M (MN)^{1.52}\right).\end{aligned} \tag{A9}$$

A similar expression holds for N_2O:

$$\begin{aligned}\mathrm{RF}(\mathrm{N_2O}) = 0.12 &\left[\sqrt{\mathrm{N_2O}(t)} - \sqrt{\mathrm{N_2O}(t_0)} \right] \\ &- f[\mathrm{CH_4}(t_0), \mathrm{N_2O}(t)] - f[\mathrm{CH_4}(t_0), \mathrm{N_2O}(t_0)].\end{aligned} \tag{A10}$$

Radiative forcing by tropospheric ozone, SF_6, the gases controlled under the Montreal Protocol, and the other halocarbons included in this model is calculated by the expression

$$\mathrm{RF} = \alpha[C(t) - C(t_0)], \tag{A11}$$

where C is the concentration (in ppb (DU for O_3)) and α is the radiative efficiency (in W m^{-2} per ppb or per DU for O_3; Table A1).

The radiative forcing due to the stratospheric O_3 depletion is calculated as a function of equivalent effective stratospheric chlorine (EESCl) (in ppb) as taken from WMO/UNEP, chapter 11 [*UNEP/WMO*, 1998]. Important bromines are taken into account in the WMO/UNEP data. Thus

$$\mathrm{RF}[\mathrm{O_3(stratosphere)}] = \alpha[\mathrm{EESCl}(t) - \mathrm{EESCl}(1970)], \tag{A12}$$

where α is in W m^{-2} ppb^{-1}.

Finally, the small radiative forcing from changing concentrations in stratospheric H_2O due to CH_4 oxidation is estimated to be 5% of the pure radiative forcing by CH_4:

$$\mathrm{RF}(\mathrm{H_2O}) = 0.05\left[0.036\left(\sqrt{\mathrm{CH_4}(t)} - \sqrt{\mathrm{CH_4}(t_0)}\right)\right]. \tag{A13}$$

A3. Radiative Forcing by Aerosols

The magnitude of radiative forcing by aerosols is not well understood and uncertain [e.g., *Penner et al.*, 2001; *Ramaswamy et al.*, 2001; *Houghton et al.*, 1996; *Shine and Forster*, 1999]. Its quantification using complex models or by simplified expressions approximating model results is highly tentative. Our motivation to estimate aerosol forcings from emissions of aerosols and aerosol precursors is to take into account at least at first order their significant contribution to the total radiative forcing of all anthropogenic agents on the global scale. We note that aerosol forcing varies strongly between different regions. Here we rely on published expressions and best estimates for present-day forcing [*Ramaswamy et al.*, 2001; *Harvey et al.*, 1996; *Shine and Forster*, 1999].

Direct radiative forcing by sulphate aerosols is taken to be proportional to anthropogenic sulphur emissions, eSO_x (in Tg S yr^{-1}) with an RF of -0.4 W m^{-2} for today:

$$\mathrm{RF}(\mathrm{S-direct}) = -0.4\ \mathrm{W\ m^{-2}} \frac{e\mathrm{SO}_x(t)}{e\mathrm{SO}_x(2000)}. \tag{A14}$$

Indirect aerosol effects via changing cloud properties are approximated as a function of sulphur emissions [*Harvey et al.*, 1996]

$$\begin{aligned}\mathrm{RF}(\mathrm{S-indirect}) = -0.8\ \mathrm{W\ m^{-2}}\ &\ln\frac{E\mathrm{nat} + e\mathrm{SO}_x(t)}{E\mathrm{nat}} \\ &\cdot \left(\ln\frac{E\mathrm{nat} + e\mathrm{SO}_x(2000)}{E\mathrm{nat}}\right)^{-1}.\end{aligned} \tag{A15}$$

Enat denotes natural sulphur emissions taken to be 42 Tg S.

Finally, the combined direct effect of black carbon (BC) and organic carbon (OC) from biomass burning and fossil fuel use is

Table A1. Concentrations, Lifetimes, and Radiative Efficiencies[a]

Gas	$C(t_0)$, ppb or ppt	C(2000), ppb or ppt	τ(2000), years	α, W m^{-2} ppb^{-1}
CO_2	278,600	368,000	...	see text
CH_4	742.2	1760	8.4	see text
N_2O	272.0	316	120	see text
tropo-O_3[b]	25	34	...	0.042
		Gases Controlled Under the Montreal Protocol		
CFC-11	0	267	45	0.25
CFC-12	0	535	100	0.32
CFC-113	0	85	85	0.30
CFC-114	0	16	300	0.31
CFC-115	0	9	1700	0.18
CCl4	0	92	35	0.13
CH3CCl3	0	44	4.8	0.06
HCFC-22	0	145	11.9	0.20
HCFC-141b	0	13	9.3	0.14
HCFC-142b	0	15	19	0.20
HCFC-123	0	0	1.4	0.20
CF2BrCl	0	4	11	0.30
CF3Br	0	3	65	0.32
EESCl[c]	1.25	3.28	...	−0.07317
		Other Halocarbons and SF_6		
CF4	44	82.0	50,000	0.08
C2F6	0	3.2	10,000	0.26
C4F10	0	0.0	2,600	0.33
SF6	0	4.7	3,200	0.52
HFC-23	0	15.0	260	0.16
HFC-32	0	0.0	5.0	0.09
HFC-125	0	0.0	29	0.23
HFC-134a	0	12.0	13.7	0.15
HFC-143a	0	0.0	52	0.13
HFC-152a	0	0.7	1.4	0.09
HFC-227ea	0	0.0	33	0.30
HFC-245ca	0	0.0	5.9	0.23
HFC-43-10mee	0	0.0	15.2	0.40

[a] Concentrations C at preindustrial time (t_0) taken to be nominal year 1765 and for today in parts per billion for CO_2, CH_4, N_2O and in parts per trillion for halocarbons and SF_6. Here τ; denotes lifetime (for CO_2, no single lifetime exists) and α radiative efficiency. The lifetimes of the fully fluorinated species (SF_6, CF_4, C_2F_6, and C_4F_{10}) are taken as time invariant, whereas the lifetimes of other halocarbons are scaled with tropospheric OH.

[b] Tropospheric ozone burden is given in Dobson units, and the radiative efficiency (in W m^{-2} DU^{-1}) was calculated assuming a present-day forcing of 0.378 W m^{-2}.

[c] Equivalent effective stratospheric chlorine (EESCl; including bromine components) is given in parts per billion for 1970 (t_0) and today. It is used to calculate radiative forcing from stratospheric O_3 depletion since 1970; the coefficient α relating radiative forcing and EESCl is obtained assuming a present-day forcing of −0.15 W m^{-2}.

taken to be proportional to anthropogenic emissions of CO, *e*CO, with a present-day forcing of −0.1 W m^{-2}, consistent with recent estimates [*Ramaswamy et al.*, 2001]

$$\mathrm{RF(OC + BC - direct)} = -0.1 \mathrm{W m^{-2}} \frac{e\mathrm{CO}(t)}{e\mathrm{CO}(2000)}. \qquad \text{(A16)}$$

Here the CO emissions tabulated in SRES [*Nakićenović et al.*, 2000] are offset by a constant value to yield a year 2000 emission of 1036 Tg(CO).

A4. Changes in the Fields of Surface Temperature, Precipitation, Cloud Cover, and Ocean Thermal Expansion

The spatiotemporal response of an AOGCM to an increase in radiative forcing can be captured by a combination of IRFs that take into account the inertia in the climate system and EOFs that describe the spatial patterns of climate change. Here we apply an IRF-EOF substitute of the ECHAM3/LSG AOGCM to project the evolution of surface temperature, precipitation, cloud cover, and ocean thermal expansion [*Hooss et al.*, 1999, *Hooss et al.*, 2001].

Hooss et al. [1999] have applied an empirical orthogonal function analysis to extract the climate change signal from an 850 year simulation of the ECHAM3/LSG where atmospheric CO_2 was prescribed to rise exponentially to reach a value four-fold of the preindustrial value at model year 120; afterward, CO_2 was kept constant [*Voss and Mikolajewicz*, 2001]. The perturbation of a climate variable, $\Delta\upsilon$, is represented as the superposition of a set of mutually orthogonal spatial patterns, $\mathrm{EOF}_i^{\Delta\upsilon}(\mathbf{x})$ and the time-dependent scalar coefficients termed principal components, $\mathrm{PC}_i^{\Delta\upsilon}(t)$:

$$\Delta v(\mathbf{x}, t) = \sum_i \mathrm{PC}_i^{\Delta v}(t)\mathrm{EOF}_i^{\Delta v}(\mathbf{x}). \qquad \text{(A17)}$$

Each of the PC-EOF pairs i is computed from the AOGCM output in successive order to explain the maximum possible variance in a climate variable.

In the substitute the global mean perturbation since preindustrial time (t_0) of each climate variable $\Delta\upsilon_{av}(t)$ is calculated from the

Table A2. Parameters of the IRF-EOF substitute of ECHAM3/LSG[a]

Variable	a_1^{υ}	a_2^{υ}	τ_1^{υ}, years	τ_2^{υ}, years	S^{υ}	S_{2x}^{υ}
Temperature	0.290	0.710	448	14.4	0.674	2.5°C
Precipitation	0.345	0.655	1098	35.0	17.3	64 mm yr^{-1}
Cloud cover	0.218	0.782	391	12.0	−0.238	−0.88%
Thermal expansion	0.960	0.040	836	31.0	34.5	128 cm

[a] Here a_i^{υ} and τ_i^{υ} are the coefficients used to calculate the impulse response function. The climate sensitivity S^{υ} is given in °C $(W\ m^{-2})^{-1}$ for surface temperature, in mm yr^{-1} $(W\ m^{-2})^{-1}$ for precipitation, in % $(W\ m^{-2})^{-1}$ for cloud cover, and in cm $(W\ m^{-2})^{-1}$ for thermal expansion. S_{2x}^{υ} is the climate sensitivity for a doubling of CO_2.

convolution integral of the appropriate IRF R^{υ} and the change in radiative forcing (RF):

$$\Delta v_{av}(t) = S^{v} \int_{t_0}^{t} dt' [R^{v}(t-t')] \left(\frac{d}{dt'} \mathrm{RF}(t') \right). \tag{A18}$$

S^{υ} is the climate sensitivity expressed as equilibrium change in $\Delta\upsilon_{av}$ for a change in RF of 1 W m^{-2} (Table A2). The change in υ at location $\mathbf{x}$ and time t is

$$\Delta v(\mathbf{x}, t) = \left[\Delta v_{av}(t) \right] \mathrm{EOF}_1^{\Delta v}(\mathbf{x}), \tag{A19}$$

when $\mathrm{EOF}_1^{\Delta\upsilon}$ is normalized to yield unity when averaged over the globe. The (normalized) IRFs, R^{υ}, to a step increase in radiative forcing are expressed analytically by

$$R^{v}(t) = \sum_i a_i^{v} \left[1 - \exp\left(\frac{-t}{\tau_i^{v}} \right) \right]. \tag{A20}$$

The coefficients of R^{υ} (equation (A20) and Table A2) were determined such as to minimize the sum of the squared deviations between the values of $\Delta\upsilon_{av}(t)$ (from (A18)) and $PC_1^{\Delta\upsilon}$ from the 850 year transient AOGCM simulation.

The substitute is built from the first EOF-PC pair only. Only the first EOF-PC pair of each of the four climate variables showed a long-term trend identifying them as climate change signal. The first EOF and PC capture 97% of the variability in near-surface temperature, 43% of the variability in cloud cover, and 31% of the variability in precipitation. Changes in the frequency of extreme events such as droughts and other changes in the variability of precipitation and cloud cover not described by the first EOF-PC pair are neglected in the substitute. Radiative forcing in the substitute is taken to be the sum of global mean radiative forcing from GHGs and aerosols, whereas the IRF-EOF pairs were determined from a CO_2 only simulation. This approximation seems justified because the correlation between the fields obtained from GHG only simulations and from simulations with GHGs and aerosols for a distinct AOGCM is, in general, higher than the correlation between output fields obtained with different AOGCMs.

A5. Atmospheric CO_2 and Oceanic Carbon Uptake

Atmospheric CO_2, pCO_{2a}, is projected from the following budget equation:

$$\frac{dpCO_{2a}}{dt} = F_{\mathrm{fossil}} + F_{\mathrm{land-use}} - F_{ab} - F_{as}. \tag{A21}$$

F_{fossil} and $F_{\mathrm{land\text{-}use}}$ represent emissions by fossil fuel burning and by land use changes. F_{ab} and F_{as} denote the uptake of excess carbon by the land biosphere as calculated with the LPJ-DGVM and the ocean. All fluxes are expressed in units of ppm yr^{-1} (1 ppm = 2.123 × 10^{15} g C = 7.779 ×10^{15} g CO_2 = 1.768 × 10^{14} mol).

The oceanic uptake is either calculated by the HILDA model or its impulse response representation [*Joos et al.*, 1996]. In the mixed layer impulse response substitute, ocean uptake is

$$F_{as} = K_g (pCO_{2a} - pCO_{2s}). \tag{A22}$$

K_g represents the global average gas exchange coefficient that is $(9.06\ \mathrm{years})^{-1}$ for HILDA, and pCO_{2a} and pCO_{2s} correspond to the global average partial pressures of CO_2 in the atmosphere and the surface ocean (expressed in units of ppm); total pressure at sea level is taken to be 1 atm. The perturbation in dissolved inorganic carbon in the surface ocean $\delta\Sigma CO_2$ is obtained from the convolution integral of the mixed layer impulse response function r_s and the net air-to-sea flux F_{as}:

$$\delta\Sigma CO_2 = \frac{c}{hA_{OC}} \int_{t_0}^{t} F_{as}(t') r_s(t-t') \mathrm{d}t', \tag{A23}$$

where h is the mixed layer depth taken to be 75 m, A_{oc} is the ocean area taken to equal 3.62 × 10^{14} m^2, and c is a unit conversion factor (c = 1.722 × 10^{17} μmol m^3 ppm^{-1} kg^{-1}).

The relationship between the perturbation in the sea surface partial pressure relative to the preindustrial temperature, T_0, and inorganic carbon is obtained by the following expression that holds for $0 \le \delta pCO_{2s} \le 1320$ ppm and 17.7°C $\le T_0 \le$ 18.3:

$$\begin{aligned} \delta pCO_{2s}(T_0) = {} & \left(1.5568 - 1.3993 T_0 \times 10^{-2}\right) \delta\Sigma CO_2 \\ & + (7.4706 - 0.20207 T_0) \times 10^{-3} (\delta\Sigma CO_2)^2 \\ & - (1.2748 - 0.12015 T_0) \times 10^{-5} (\delta\Sigma CO_2)^3 \\ & + (2.4491 - 0.12639 T_0) \times 10^{-7} (\delta\Sigma CO_2)^4 \\ & - (1.5468 - 0.15326 T_0) \times 10^{-10} (\delta\Sigma CO_2)^5. \end{aligned} \tag{A24}$$

The preindustrial global average surface ocean temperature T_0 is taken to be 18.2°C, and δpCO_{2s} and $\delta\Sigma CO_2$ are again in units of ppm and μmol kg^{-1}. The CO_2 partial pressure increases exponentially with sea surface temperature [*Takahashi et al.*, 1993], and we estimate sea surface partial pressure at time t to be

$$pCO_{2s}(t) = [pCO_{2s}(t_0) + \delta pCO_{2s}(T_0)] \exp\left(0.0423\ \mathrm{K}^{-1} \Delta T\right). \tag{A25}$$

Here $pCO_{2s}(t_0)$ is the preindustrial sea surface pressure taken to be equal the atmospheric pressure, and ΔT is the perturbation in global mean sea surface pressure, here calculated with the IRF-EOF substitute of the ECHAM3/LSG. This approximation gives similar results for the reduction in oceanic carbon uptake by SST warming as found for spatially resolved models (see Figure 3 of *Joos et al.* [1999b] and *Plattner et al.* [2001]).

Finally, the mixed layer impulse response r_s for the HILDA model is, for $0 \leq t \leq 2$ years,

$$r_s(t) = 0.12935 + 0.21898 \exp(-t/0.034569) + 0.17003 \exp(-t/0.26936) + 0.24017 \exp(-t/0.96083) + 0.24093 \exp(-t/4.9792) \quad \text{(A26)}$$

(check value: r_s(t = 2 years) = 0.32071), and for $t \geq 2$ years is

$$r_s(t) = 0.022936 + 0.24278 \exp(-t/1.2679) + 0.13963 \exp(-t/5.2528) + 0.089318 \exp(-t/18.601) + 0.037820 \exp(-t/68.736) + 0.035549 \exp(-t/232.30) \quad \text{(A27)}$$

(check value: r_s(t = 2 years) = 0.32068).

Acknowledgments. We thank Michael Prather for generously providing an algorithm to project reactive greenhouse gas concentrations from emissions. Comments by Bob Scholes and Martin Heimann were much appreciated. This work was supported by the Swiss National Science Foundation and by the Carbon Cycle Model Linkage Project (CCMLP) of the Electric Power Research Institute (Palo Alto).

References

Battle, M., M. L. Bender, P. P. Tans, J. M. C. White, J. T. Ellis, T. Conway, and R. J. Francey, Global carbon sinks and their variability inferred from atmospheric CO_2 and ^{13}C, *Science*, *287*, 2467–2470, 2000.

Birks, H. H., and B. Ammann, Two terrestrial records of rapid climatic change during the glacial-Holocene transition (14,000–9,000 calender years B.P.) from Europe, *Proc. Natl. Acad. Sci. USA*, *97*, 1390–1394, 2000.

Cao, M., and F. I. Woodward, Dynamic responses of terrestrial ecosystem carbon cycling to global climate change, *Nature*, *393*, 249–251, 1998.

Caspersen, J. P., S. W. Pacala, J. C. Jenkins, G. C. Hurtt, P. R. Moorcroft, and R. A. Birdsey, Contributions of land-use history to carbon accumulation in U.S. forests, *Science*, *290*, 1148–1151, 2000.

Cooperative Holocene Mapping Project (COHMAP) Members, Climate changes of the last 18,000 years: Observations and model simulations, *Science*, *241*, 1043–1052, 1988.

Covey, C., K. M. Achuta Rao, S. J. Lambert, and K. E. Taylor, Intercomparison of present and future climates simulated by coupled ocean-atmosphere GCMs, *PCMDI Rep. 66*, Program for Clim. Model Diagnosis and Intercomparison, Lawrence Livermore Natl. Lab., Univ. of Calif., Livermore, 2000.

Cox, P., R. Betts, C. Jones, S. Spall, and I. Totterdell, Will carbon-cycle feedbacks accelerate global warming in the 21st century?, *Nature*, *408*, 184–187, 2000.

Cramer, W., et al., Global response of terrestrial ecosystem structure and function to CO_2 and climate change: Results from six dynamic global vegetation models, *Global Change Biol.*, *7*, 357–373, 2001.

Crowley, T. J., Ice age terrestrial carbon changes revisited, *Global Biogeochem. Cycles*, *9*, 377–389, 1995.

Cubasch, U. R., R. Voss, G. C. Hegerl, J. Waszkewitz, and T. J. Crowley, Simulation of the influence of solar radiation variations on the global climate with an ocean-atmosphere general circulation model, *Clim. Dyn.*, *13*, 757–767, 1997.

Dai, A., and I. Y. Fung, Can climate variability contribute to the "missing" CO_2 sink?, *Global Biogeochem. Cycles*, *7*, 599–609, 1993.

Dixon, R. K., S. Brown, R. A. Houghton, A. M. Solomon, M. C. Trexler, and J. Wisniewski, Carbon pools and flux of global forest ecosystems, *Science*, *263*, 185–190, 1994.

Etheridge, D. M., L. P. Steele, R. L. Langenfelds, R. J. Francey, J.-M. Barnola, and V. I. Morgan, Natural and anthropogenic changes in atmospheric CO_2 over the last 1000 years from air in Antarctic ice and firn, *J. Geophys. Res.*, *101*, 4115–4128, 1996.

Farquhar, G. D., S. von Caemmerer, and J. A. Berry, A biochemical model of photosynthetic CO_2 assimilation in leaves of C_3 species, *Planta*, *149*, 78–90, 1980.

Foley, J., An equilibrium model of the terrestrial carbon budget, *Tellus, Ser. B.*, *47*, 310–319, 1995.

Folland, C. K., T. R. Karl, J. R. Christy, R. A. Clarke, G. V. Gruza, J. Jouzel, M. E. Mann, J. Oerlemans, M. J. Salinger, and S.-W. Wang, Observed climate variability and change, in *Climate Change 2001: The Scientific Basis, Contribution of Working Group I to the Third Assessment Report of the Intergovernmental Panel on Climate Change*, edited by J. T. Houghton et al., pp. 99–181, Cambridge Univ. Press, New York, 2001.

Giardina, C., and M. Ryan, Evidence that decomposition rates of organic carbon in mineral soil do not vary with temperature, *Nature*, *404*, 858–861, 2000.

Hansen, J., A. Lacis, D. Rind, G. Russell, P. Stone, I. Fung, R. Ruedy, and J. Lerner, Climate sensitivity: Analysis of feedback mechanisms, in *Climate Processes and Climate Sensitivity, Geophys. Monogr. Ser.*, vol. 29, pp. 130–163, AGU, Washington, D. C., 1984.

Harvey, L. D., J. Gregory, M. Hoffert, A. Jain, M. Lal, R. Leemans, S. Raper, T. Wigley, and J. de Wolde, An introduction to simple climate models used in the IPCC Second Assessment Report, *IPCC Tech. Pap. II*, Intergovt. Panel on Clim. Change, 1996.

Hättenschwiler, S., F. Miglietta, A. Raschi, and C. Körner, Thirty years of in situ tree growth under elevated CO_2: A model for future forest responses, *Global Change Biol.*, *3*, 463–471, 1997.

Haxeltine, A., and I. C. Prentice, BIOME 3: An equilibrium terrestrial biosphere model based on ecophysiological constraints, resource availability, and competition among plant functional types, *Global Biogeochem. Cycles*, *10*, 693–703, 1996.

Hooss, G., R. Voss, K. Hasselmann, E. Maier-Reimer, and F. Joos, A nonlinear impulse response model of the coupled carbon cycle-ocean-atmosphere climate system, *Tech. Rep. 290*, Max-Planck-Inst. für Meteorol., Hamburg, Germany, 1999.

Hooss, G., R. Voss, K. Hasselmann, K., E. Maier-Reimer, and F. Joos, A nonlinear impulse response model of the coupled carbon cycle-ocean-atmosphere climate system, *Clim. Dyn.*, in press, 2001.

Houghton, J. T., L. G. M. Filho, B. A. Callander, N. Harris, A. Kattenberg, and K. Maskell, *Climate Change 1995—Science of Climate Change: Contribution of WGI to the Second Assessment Report of the Intergovernmental Panel on Climate Change*, Cambridge Univ. Press, New York, 1996.

Houghton, R. A., The annual net flux of carbon to the atmosphere from changes in land use 1850–1990, *Tellus, Ser. B*, *51*, 298–313, 1999.

Huntingford, C., and P. Cox, An analogue model to derive additional climate change scenarios from existing GCM simulations, *Clim. Dyn.*, *16*, 575–586, 2000.

Jarvis, P., and S. Linder, Botany — Constraints to growth of boreal forests, *Nature*, *405*, 904–905, 2000.

Joos, F., and M. Bruno, Long-term variability of the terrestrial and oceanic carbon sinks and the budgets of the carbon isotopes ^{13}C and ^{14}C, *Global Biogeochem. Cycles*, *12*, 277–295, 1998.

Joos, F., M. Bruno, R. Fink, T. F. Stocker, U. Siegenthaler, C. Le Quéré, and J. L. Sarmiento, An efficient and accurate representation of complex oceanic and biospheric models of anthropogenic carbon uptake, *Tellus, Ser. B*, *48*, 397–417, 1996.

Joos, F., J. C. Orr, and U. Siegenthaler, Ocean carbon transport in a box-diffusion versus a general circulation model, *J. Geophys. Res.*, *102*, 12,367–12,388, 1997.

Joos, F., R. Meyer, M. Bruno, and M. Leuenberger, The variability in the carbon sinks as reconstructed for the last 1000 years, *Geophys. Res. Lett.*, *26*, 1437–1441, 1999a.

Joos, F., G.-K. Plattner, T. F. Stocker, O. Marchal, and A. Schmittner, Global warming and marine carbon cycle feedbacks on future atmospheric CO_2, *Science*, *284*, 464–467, 1999b.

Keeling, C. D., and T. P. Whorf, Atmospheric CO_2 records from sites in the SIO network, in *Trends '93: A Compendium of Data on Global Change*, edited by T. Boden et al., pp. 16–26, Carbon Dioxide Inf. Anal. Cent., Oak Ridge, Tenn., 1994.

Keeling, R. F., S. C. Piper, and M. Heimann, Global and hemispheric CO_2 sinks deduced from changes in atmospheric O_2 concentration, *Nature*, *381*, 218–221, 1996.

Leemans, R., and W. Cramer, The IIASA climate database for land areas on a grid with 0.5° resolution, *Res. Rep. RR-91-18.*, Int. Inst. for Appl. Syst. Anal., Laxenburg, Austria, 1991.

Lloyd, J., and J. A. Taylor, On the temperature dependence of soil respiration, *Functional Ecol.*, *8*, 315–323, 1994.

Luo, Y., J. Reynolds, and Y. Wang, A search for predictive understanding of plant responses to elevated CO_2, *Global Change Biol.*, *5*, 143–156, 1999.

MacDonald, G. M., R. W. D. Edwards, K. A. Moser, R. Pienitz, and J. P. Smol, Rapid response of treeline vegetation and lakes to past climate warming, *Nature*, *361*, 243–246, 1993.

Maier-Reimer, E., U. Mikolajewicz, and A. Winguth, Future ocean uptake of CO_2: Interaction between ocean circulation and biology, *Clim. Dyn.*, *12*, 711–721, 1996.

Marland, G., T. A. Boden, and R. J. Andres, Global, regional and national annual CO_2 emission estimates from fossil-fuel burning, hydraulic-cement production and gas flaring: 1950 to 1992, *CDIAC Commun., Fall*, 20–21, 1995.

Matear, R. J., and A. C. Hirst, Climate change feedback on the future oceanic CO_2 uptake, *Tellus, Ser. B*, *51*, 722–733, 1999.

Mayle, F., and L. Cwyner, Impact of the Younger Dryas cooling event upon lowland vegetation of Maritime Canada, *Ecol. Monogr.*, *65*, 129–154, 1995.

McGuire, A.D., et al., Carbon balance of the terrestrial biosphere in the twentieth century: Analyses of CO_2, climate, and land-use effects with four process-based ecosystem models, *Global Biogeochem. Cycles*, *15*, 183–206, 2001.

Meehl, G. A., G. J. Boer, C. Covey, M. Latif, and R. J. Stouffer, The Coupled Model Intercomparison Project (CMIP), *Bull. Am. Meteorol. Soc.*, *81*, 313–318, 2000.

Meyer, R., F. Joos, G. Esser, M. Heimann, G. Hooss, G. Kohlmaier, W. Sauf, R. Voss, and U. Wittenberg, The substitution of high-resolution terrestrial biosphere models and carbon sequestration in response to changing CO_2 and climate, *Global Biogeochem. Cycles*, *13*, 785–802, 1999.

Monteith, J. L., Accomodation between transpiring vegetation and the convective boundary layer, *J. Hydrol.*, *166*, 251–263, 1995.

Myhre, G., E. J. Highwood, K. P. Shine, and F. Stordal, New estimates of radiative forcing due to well mixed greenhouse gases, *Geophys. Res. Lett.*, *25*, 2715–2718, 1998.

Nakićenović, et al., *Special Report on Emission Scenarios*, Cambridge Univ. Press, New York, 2000.

Neftel, A., E. Moor, H. Oeschger, and B. Stauffer, Evidence from polar ice cores for the increase in atmospheric CO_2 in the past two centuries, *Nature*, *315*, 45–47, 1985.

Penner, J. A., et al., Aerosols, their direct and indirect effects, in *Climate Change 2001: The Scientific Basis, Contribution of Working Group I to the Third Assessment Report of the Intergovernmental Panel on Climate Change*, edited by J. T. Houghton et al., pp. 289–348, Cambridge Univ. Press, New York, 2001.

Plattner, G.-K., F. Joos, T. F. Stocker, and O. Marchal, Feedback mechanisms and sensitivities of ocean carbon uptake under global warming, *Tellus*, *Ser. B, 53*, 564–592, 2001.

Prather, M., et al., Atmospheric chemistry and greenhouse gases, in *Climate Change 2001: The Scientific Basis, Contribution of Working Group I to the Third Assessment Report of the Intergovernmental Panel on Climate Change*, edited by J. T. Houghton et al., pp. 239–287, Cambridge Univ. Press, New York, 2001.

Prentice, I. C., P. Bartlein, and T. I. Webb, Vegetation change in eastern North America since the Last Glacial Maximum: A response to continuous climatic forcing, *Ecology*, *72*, 2038–2056, 1991.

Prentice, I. C., M. Heimann, and S. Sitch, The carbon balance of the terrestrial biosphere: Ecosystem models and atmospheric observations, *Ecol. Appl.*, *10*, 1553–1573, 2000.

Ramaswamy, V., O. Boucher, J. Haigh, D. Hauglustaine, J. Haywood, G. Myhre, T. Nakajima, G. Y. Shi, and S. Solomon, Radiative forcing of climate change, in *Climate Change 2001: The Scientific Basis, Contribution of Working Group I to the Third Assessment Report of the Intergovernmental Panel on Climate Change*, edited by J. T. Houghton et al., pp. 349–416, Cambridge Univ. Press, New York, 2001.

Rustad, L., Warming effects on ecosystem functioning, *Newsl. Global Change Terr. Ecosyst. Core Proj. IGBP*, *16*, 4–5, 2000.

Sarmiento, J. L., and C. Le Quéré, Oceanic carbon dioxide uptake in a model of century-scale global warming, *Science*, *274*, 1346–1350, 1996.

Schindler, D. W., and S. E. Bayley, The biosphere as an increasing sink for atmospheric carbon: Estimates from increased nitrogen deposition, *Global Biogeochem. Cycles*, *7*, 717–733, 1993.

Shine, K. P., and P. Forster, The effect of human activity on radiative forcing of climate change: A review of recent developments, *Global Planet. Change*, *20*, 205–225, 1999.

Shine, K., R. G. Derwent, D. J. Wuebbles, and J.-J. Morcrette, Radiative forcing of climate, in *Climate Change: The IPCC Scientific Assessment*, edited by J. T. Houghton, G. J. Jenkins, and J. J. Ephraums, pp. 41–68, Cambridge Univ. Press, New York, 1990.

Shine, K., Y. Fouquart, V. Ramaswamy, S. Solomon, and J. Srinivasan, Radiative forcing, in *Climate Change 1994: Radiative Forcing of Climate Change and an Evaluation of the IPCC IS92 Emission Scenarios*, edited by J. T. Houghton et al., pp. 163–203, Cambridge Univ. Press, New York, 1994.

Siegenthaler, U., and F. Joos, Use of a simple model for studying oceanic tracer distributions and the global carbon cycle, *Tellus, Ser. B*, *44*, 186–207, 1992.

Sitch, S., *The role of vegetation dynamics in the control of atmospheric CO_2 content*, Ph.D. thesis, Lund Univ., Lund, Sweden, 2000.

Smith, T. M., and H. H. Shugart, The transient response of terretrial carbon storage to a perturbed climate, *Nature*, *361*, 523–526, 1993.

Takahashi, T., J. Olafsson, J. G. Goddard, D. W. Chipman, and S. C. Sutherland, Seasonal variation of CO_2 and nutrients in the high-latitude surface oceans: A comparative study, *Global Biogeochem. Cycles*, *7*, 843–878, 1993.

Townsend, A. R., B. H. Braswell, E. A. Holland, and J. E. Penner, Spatial and temporal patterns in terrestrial carbon storage due to the deposition of fossil fuel nitrogen, *Ecol. Appl.*, *6*, 806–814, 1996.

Trumbore, S. E., O. A. Chadwick, and R. Amundson, Rapid exchange between soil carbon and atmospheric carbon dioxide driven by temperature change, *Science*, *272*, 393–396, 1996.

United Nations Environment Programme/World Meteorological Organization (UNEP/WMO), Scientific assessment of ozone depletion, *Global Ozone Res. Monitor. Proj. Rep. 44*, 732 pp., World Meteorol. Org., Geneva, Switzerland, 1998.

Voss, R., and U. Mikolajewicz, Long-term climate changes due to increased CO_2 concentration in the coupled atmosphere-ocean general circulation model ECHAM3/LSG, *Tech. Rep. 298*, Max-Planck Inst. für Meteorol., Hamburg, Germany, 1999.

Voss, R., and U. Mikolajewicz, Long-term climate changes due to increased CO_2 concentration in the coupled atmosphere-ocean general circulation model ECHAM3/LSG, *Clim. Dyn.*, *17*, 45–60, 2001.

Voss, R., R. Sausen, and U. Cubasch, Periodically synchonously coupled integrations with the atmosphere-ocean general circulation model ECHAM3/LSG, *Clim. Dyn.*, *14*, 249–266, 1998.

S. Gerber, F. Joos, R. Meyer, and G.-K. Plattner, Climate and Environmental Physics, Physics Institute, University of Bern, Sidlerstrasse 5, CH-3012 Bern, Switzerland. (gerber@climate.unibe.ch; joos@climate.unibe.ch; meyer@climate.unibe.ch; plattner@climate.unibe.ch)

K. Hasselmann and G. Hooss, Max Planck Institute for Meteorology, Bundesstrasse 55, D-20146 Hamburg, Germany. (klaus.hasselmann@dkrz.de; hooss@dkrz.de)

I. C. Prentice, Max Planck Institute for Biogeochemistry, Tatzendpromenade 1a, Postfach, 100164, D-07701 Jena, Germany. (cprentic@bgc-jena.mpg.de)

S. Sitch, Potsdam Institute for Climate Impact Research, P.O. Box 601203, D-14412 Potsdam, Germany. (sitch@pik-potsdam.de)

(Received November 22, 2000; revised May 14, 2001;
accepted June 26, 2001.)